PCCP

Accepted Manuscript

This is an *Accepted Manuscript*, which has been through the Royal Society of Chemistry peer review process and has been accepted for publication.

Accepted Manuscripts are published online shortly after acceptance, before technical editing, formatting and proof reading. Using this free service, authors can make their results available to the community, in citable form, before we publish the edited article. We will replace this *Accepted Manuscript* with the edited and formatted *Advance Article* as soon as it is available.

You can find more information about *Accepted Manuscripts* in the **Information for Authors**.

Please note that technical editing may introduce minor changes to the text and/or graphics, which may alter content. The journal's standard **Terms & Conditions** and the **Ethical guidelines** still apply. In no event shall the Royal Society of Chemistry be held responsible for any errors or omissions in this *Accepted Manuscript* or any consequences arising from the use of any information it contains.

"Heteronuclear DNP of Protons and Deuterons with TEMPOL"

Kaminker I. [+a], Shimon D. [+], Hovav Y. [b], Feintuch A., and Vega S.*

Weizmann institute of Science, Rehovot , Israel

[a] present address: Department of Chemistry and Biochemistry, University of California, Santa Barbara, U.S.A.

[b] present address: Department of Applied Physics, Hebrew University of Jerusalem, Israel

*Shimon.Vega@weizmann.ac.il

[+]equal contributions

1 Introduction

Dynamic nuclear polarization (DNP) is a popular technique for signal enhancement in Nuclear Magnetic Resonance (NMR) spectroscopy. DNP is a collective designation for a number of different though related techniques, all resulting in transfer of polarization from highly polarized electrons to weaker polarized nuclei thus enhancing the NMR signal of the latter. In DNP on non-conducting solids, four mechanisms are usually recognized: The Solid Effect (SE), the Cross Effect (CE), where we make a distinction between the direct CE (dCE) and indirect CE (iCE), Thermal Mixing (TM) and the Overhauser Effect (OE). During the SE mechanism spin polarization is transferred from single electrons to the hyperfine coupled nuclei, mediated by a microwave (MW) irradiation on the "forbidden" zero quantum (ZQ) or double quantum (DQ) transitions [1, 2, 3, 4, 5, 6, 7, 8, 9]. The CE involves two dipolar coupled electrons that transfer their polarization to the hyperfine coupled nuclei. This happens when the difference between the frequencies of the two coupled electrons in an inhomogeneously broadened EPR line becomes about equal to the nuclear Larmor frequency (the CE condition). Then, strong electron-nuclear spin state mixing occurs and irradiation of the allowed electron transitions results in a significant increase of the dCE-induced polarization transfer efficiency[10, 11, 12, 13, 14, 15, 16, 17, 18]. The iCE involves nuclear polarization generated by all pairs of electrons at a CE condition when the two electrons have different polarizations [13, 19]. These polarization differences are formed, in general, via partial saturation of the EPR spectrum due to MW irradiation and electron Spectral Diffusion (eSD) [20, 21, 22, 23, 24, 25, 26]. The TM formalism

describes the DNP polarization transfer between the bath of coupled electrons and the interacting nuclei in terms of thermodynamic arguments and spin temperature concepts. In the case where the electron spin bath exhibits a broad EPR line, the polarization of the ensemble of all coupled nuclei (the nuclear bath) in the sample is enhanced by a process equilibrating its nuclear spin temperature to the "non-Zeeman" electron spin temperature induced by the MW irradiation [2, 8, 27, 28, 29, 30, 31, 32, 33, 34]. Finally, the OE is usually the enhancement mechanism that takes place in metallic or liquid samples [35, 36, 37, 38] , and was recently shown to be efficient as well in non-conducting solids [39, 40]. OE-DNP enhancement is the result of an on-resonance MW irradiation on an electron that polarizes its coupled nuclei when there exists an imbalance between the DQ and ZQ electron-nucleus cross-relaxation rates [39, 40, 41, 42, 43, 44].

Somewhat surprising for a field with a well-developed theoretical background, is the fact that some of the modern DNP results can not yet be explained with the available DNP formalisms. It has been common notion that under the conditions typically employed for sample polarization in dissolution DNP experiments (direct polarization of ^{13}C nuclei from narrow line trityl radicals at very low temperatures ~1.5K and modest magnetic field of ~3.5T) the dominant enhancement mechanism is TM [8, 45, 46, 47, 48, 49, 50]. However, the exact shapes of the frequency swept DNP spectra could not be reproduced using the common TM formalism [46, 47, 48, 49, 51, 52].

Many of the static dissolution DNP experiments employ trityl radicals that generate high ^{13}C signal enhancements. Nitroxide radicals were also used during these experiments since they pose some advantages over trityl, such as lower price, ease at which they can be removed from solutions [53] and large ^{1}H polarization that can be transferred to ^{13}C nuclei via cross polarization [54, 55]. Such nitroxide radicals were subject of numerous studies, aiming at understanding the underlying DNP mechanism and subsequently improving the DNP enhancement [24, 40, 45, 47, 49, 50, 56, 57, 58, 59, 60, 61]. In this framework modern DNP experimental results were explained using TM [40, 45, 46, 47, 48, 49, 56, 57, 62, 63] or alternatively using quantum mechanical approaches representing the SE and CE mechanisms [59, 60, 64, 65]. The latter focused largely on ^{1}H- or ^{13}C-DNP and resulted in quantitative decompositions of the experimental DNP spectra in terms of SE and CE contributions and later iCE contributions [61]. In this work we extend these studies by considering simultaneously two types of nuclei, ^{1}H and ^{2}H, present in the system.

Samples with several types of magnetic nuclei sometimes exhibit experimental evidence of a cross-talk between the nuclei, such as different nuclei having DNP enhancement spectra with similar shapes and different nuclei showing polarization exchange even without MW irradiation. These types of effects are seen in samples where the coupled nuclei have Larmor frequencies that are smaller than the EPR linewidth, as for example in Refs. [2, 28, 29, 45, 46, 49, 51, 52, 56, 66, 67, 68, 69, 70, 71, 72] and in others. Such an exchange between nuclear polarizations was, for example, demonstrated in Ref. [67], where DNP

experiments were performed on a sample containing ^{19}F and ^{7}Li nuclei. There it was shown that, when after the DNP enhancement of both ^{19}F and ^{7}Li the MW irradiation was switched off and the ^{7}Li nuclei were saturated, its polarization partially recovered on account of the ^{19}F polarization. This effect was explained by relying on a ^{7}Li-^{19}F coupling mediated by the electrons. In the literature these polarization transfer phenomena are described using the TM formalism, because it predicts that all the nuclei will at steady state reach the same spin temperature. As a result they will reach the same enhancement values and thus have the same shape of the DNP spectrum [2, 32, 52].

Recently we showed, based on simulations of the spin evolution in small model systems, that similar "cross-talk" effects between two types of nuclei can possibly be explained using a heteronuclear (hnCE) DNP mechanism [61]. This nuclear polarization exchange mechanism can take place in the vicinity of coupled electron pairs with resonance frequency differences that match the sum or difference of the Larmor frequencies of two types of nuclei in the sample. In particular these simulations have shown that this hnCE mechanism can cause a partial recovery of the hyperpolarization of one type of the nuclei after its saturation at the expense of the polarization of the other type, thus resembling the experimental results.

Here we demonstrate that the DNP spectra of both ^{1}H and ^{2}H nuclei in a sample composed of 50% v/v ^{1}H$_2$O/DMSO-d$_6$ and containing 40 mM TEMPOL can become identical at sufficiently low temperatures (<6 K) and that there exists an efficient polarization exchange between the two nuclear pools at this temperature. All these are hallmark predictions of the TM theory. However, the origin of these observations can not, in our case, be explained using the standard TM formalism, as in our sample the electron reservoir can not be described by a single non-Zeeman spin temperature, which is a necessary prerequisite of TM. This conclusion follows from the analysis of the ELDOR experiments on our sample and is similar to the results obtained by Hovav et al. [19, 23]. Consequently, another mechanism must be used in order to explain these "cross-talk" effects between the nuclei and we show that this is possible using the hnCE process [61].

In the present study we show that the hnCE can account for polarization transfer between two types of nuclei, and that there exists a clear relationship between the steady state polarizations of the two types in microscopic spin systems which can be correlated to the phenomenon observed in the two types of bulk nuclear signals in samples during DNP experiments. However, as of now, we do not yet have a clear theoretical framework allowing us to extend the hnCE findings in the microscopic system to the observations obtained from the bulk nuclei during our DNP experiments.

2 Experimental Methods and Simulations

2.1 Experimental Methods

2.1.1 Hardware

NMR and EPR experiments were carried out using a home-built combined EPR / NMR spectrometer [73]. All experiments were carried out at the magnetic field of ~ 3.38 T, corresponding to a ^{1}H Larmor frequency of 144 MHz, a ^{2}H Larmor frequency of 22.1MHz and an electron Larmor frequency of ~95GHz. The probe and sample were located inside a liquid He flow-cryostat and experiments were performed at 6 K and 20 K. Experiments with ^{1}H signal detection were carried out using a previously described probe with a tuning and matching circuit located outside the cryostat [73]. A new, low radio frequency (RF), probe was built and installed for detection of ^{2}H nuclei with tuning and matching capacitors positioned in close proximity to the NMR coil. This allowed for a significant increase in the available ^{2}H-RF irradiation field strength and of the ^{2}H detection sensitivity as compared to our previous design. The capacitors were bought from Polyflon Design, with a capacitance range of 0.8-5 pF. Triple resonance experiments (electron, ^{1}H, ^{2}H) with ^{1}H NMR detection (using the external tuning circuit probe) were made possible by introducing a high power RF relay (switching time ~50ms) between the probe and a pair of external tuning circuits each tuned to either ^{1}H or ^{2}H Larmor frequencies. A similar double RF tuned design was installed to enable ^{1}H irradiation for the probe with the internal ^{2}H circuitry. Here an additional tunable circuit, installed outside the cryostat, in series with the first one allowed tuning and matching to the ^{1}H frequency. A high power relay was used to switch between two states, one including the external circuit and one bypassing it, enabling tuning to the ^{1}H and ^{2}H frequencies, respectively.

2.1.2 Samples

The measurements were performed on samples that contained 40 mM TEMPOL radical dissolved in ^{2}H$_2$O / dimethyl sulfoxide (DMSO) (referred to as "D$_2$O" sample), ^{1}H$_2$O/DMSO-d$_6$ (referred to as "H$_2$O" sample), or ^{2}H$_2$O/DMSO-d$_6$ (referred to as "fully deuterated" sample). A H$_2$O/DMSO ratio of 50% v/v was used in all cases. TEMPOL and DMSO were purchased from Sigma-Aldrich, and the deuterated compounds from Cambridge Isotope Laboratories. All solvents were used without further purification or degassing of the samples. ~30µl of the sample was placed in a home-made PTFE sample holder, which was mounted on the NMR probe, and was inserted into a liquid He flow, pre-cooled cryostat. Measurements were performed at 6 K and 20 K.

2.1.3 EPR Experiments

The EPR signals were detected using an echo detection scheme (α-τ-α-τ-echo) composed of 800 nsec length MW pulses ($\alpha \approx 90^0$) and an echo delay time of $\tau = 1\mu sec$. In all cases, the strength of the MW irradiation was approximately $\omega_1 \approx 600$ kHz as measured from electron nutation experiments. The integrated intensity of the real part of the echo was recorded for all EPR experiments.

Electron spin-lattice relaxation times, T_{1e}, were measured by saturation-recovery experiments with a MW saturation pulse, $t_{sat} = 50$ msec at the frequency $\omega_{excite}/2\pi = 95$ GHz. The saturation-recovery curves were fit to a single exponent with a time constant T_{1e}.

Electron Double Resonance (ELDOR) experiments were conducted by irradiating at a varying MW frequency ω_{excite} for a time $t_{excite} = 200$ msec followed by detection of the EPR echo at a fixed frequency ω_{detect}, using a second MW channel. Several ELDOR spectra, $E_e^{exp}(\omega_{excite}, t_{excite}; \omega_{detect})$, were measured, each one with a different ω_{detect} frequency. Each $E_e^{exp}(\omega_{excite}, t_{excite}; \omega_{detect})$ spectrum was normalized with respect to the echo signal detected after a large off-resonance excitation at a ω_{excite} frequency far removed from the frequency range of the EPR spectrum.

2.1.4 DNP and NMR Experiments

The ^{1}H and ^{2}H NMR signals were detected using the solid echo sequence ($(\pi/2)_x - \tau - (\pi/2)_y$) with a two-step phase cycle. $\pi/2$ pulse lengths of 3.5 μsec and 4 μsec, were used for ^{1}H detection and ^{2}H detection, respectively. In both cases an echo delay time of $\tau = 30$ μsec was used, and the echo was integrated between its half-maximum positions. DNP experiments with ^{1}H detection were preceded by a saturation pulse train at the ^{1}H frequency and experiments with ^{2}H detection were preceded by saturation trains at both ^{1}H and ^{2}H NMR frequencies. ^{2}H buildup and decay experiments were preceded with only ^{2}H saturation. The saturation trains employed with the different NMR probes are detailed in the Supporting Information (SI). In the standard DNP experiments the saturation was followed by a MW irradiation pulse at a frequency $\omega_{excite}/2\pi$ and of a length t_{excite}, which in turn was followed by an echo detection of ^{1}H or ^{2}H. Here it is important to note that the shape of the Fourier transformed enhanced^{1}H and ^{2}H NMR signals did not change as a function of MW frequency or irradiation strength. Therefore we plot the integrated echo intensities, with fixed half-maximum integration boundaries, following all MW irradiation frequencies to obtain our DNP spectra. The thermal equilibrium signal was measured both for ^{1}H and ^{2}H and was used to estimate the enhancement. DNP spectra were measured using a constant t_{excite} and varying $\omega_{excite}/2\pi$ and detecting either of ^{1}H or ^{2}H signals.

Each individual data point of the DNP spectra is a result of an independent DNP

experiment and equals to the ratio between its enhanced NMR signal and an unenhanced signal obtained without MW pre-irradiation. It is of interest to discuss here the signal to noise ratio (SNR) of these ratios. The unenhanced NMR data were collected via signal accumulation until a SNR larger than 50 was obtained. This required typically two to fifty scans depending on temperature and the observed ^{1}H or ^{2}H nuclei. Since these unenhanced signals are small their SNR provide the biggest source of error when determining the DNP enhancement value. However they are not the limiting factor on the precision of the shapes of the DNP spectra. Observation of the DNP profiles shows that they are smooth without visible point to point fluctuations, indicating sufficient SNR for the individual NMR experiments used to construct the DNP curve. The enhanced signals for different MW frequencies have naturally high SNR ratios, but their actual values are affected to some extent by small changes in the experimental setup, such as relative positions of the horn, mirror and sample holder in the DNP probe, that can affect the effective MW power at the sample position. Here, however, we concentrated our efforts on reproducing the shapes of the DNP spectra rather than on the precise enhancement values. Repeating the DNP experiments with a span of two years revealed that the line shapes of the new DNP spectra were virtually indistinguishable from the earlier ones.

DNP buildup curves were measured using a constant $\omega_{excite}/2\pi = 94.87$ GHz and varying t_{excite}. DNP decay curves were measured using a constant t_{excite} and a constant $\omega_{excite}/2\pi = 94.87$ GHz and a varying time , t_{delay}, between the end of the MW irradiation and the time of NMR detection. More complex time domain DNP experiments designed to measure the polarization transfer between the ^{1}H and ^{2}H nuclei are described in the Results section.

2.2 Simulation Methods

Two types of simulations were performed for analyzing the experimental data. The first involves calculations of the steady state DNP profiles of macroscopic systems by deriving their shape from the experimentally determined electron polarization distribution along the EPR spectrum during MW irradiation. This method was introduced in Ref. [19, 23] and was subsequently applied to derive ^{13}C-DNP lineshapes of samples containing trityl [61].

The second type of simulations involved quantum mechanical calculations on small model spin systems at their standard CE conditions, similar to the work in Ref. [17], and at hnCE conditions [61]. These quantum mechanical calculations were performed by following the time behavior of the spin density state vector in a reduced Liouville space, where the coherence terms in the state vector were neglected, as introduced in Ref. [74].

In the rest of this work we will express the electron/MW frequencies in units of MHz,

with respect to a reference frequency $\nu_{ref} = 95$ GHz, such that instead of ω_ξ we will write $\delta\nu_\xi = \omega_\xi/2\pi - \nu_{ref}$ with $\xi = e$, *excite*, *detect* or others.

2.2.1 Simulations of the DNP spectra

The model used to calculate the DNP spectra from the electron polarization profiles is explained in detail in Refs. [19, 23, 61]. In this manuscript we give a short description of this model without explicitly showing the rate equations for the polarizations, for simplicity. In this model we calculate electron polarization profiles along the EPR spectrum during MW irradiation at various frequencies and derive from them simulated ELDOR spectra that are fitted to the experimental ELDOR spectra. The shapes of these polarization profiles, and their resulting ELDOR spectra, are determined by a set of parameters that include the spin-relaxation times, an effective hyperfine coefficient and an eSD rate coefficient. Thus here we take into account the eSD process that was missing in our earlier models [59, 60, 64, 65]. The objective of these calculations is to find a set of parameters that results in ELDOR spectra that fit the experimental ones. These parameters then define the actual electron polarization profiles from which we calculate the basic DNP lineshapes corresponding to the SE-, dCE- and iCE-DNP processes.

Calculation of electron polarization profiles

The polarization of the electrons $P_e(\delta\nu_{detect}; \delta\nu_{excite}, t_{excite})$ at different frequencies in the EPR line, $\delta\nu_{detect}$, during MW irradiation at $\delta\nu_{excite}$, can be calculated by solving a set of coupled rate equations for the polarizations $P_e(\delta\nu_j; \delta\nu_{excite}, t_{excite})$ of the electrons in fixed frequency bins j, and an average nuclear polarization P_n representing all nuclei of one type in the system. Each bin j has a frequency $\delta\nu_{detect} = \delta\nu_j$, a width of 2 MHz and a relative intensity $f(\delta\nu_i)$, composing the normalized EPR spectrum. The rate equation model includes the effects of the MW irradiation, the eSD process and the relaxation times of the electrons and nuclei. It also takes into account the EPR lineshape of the electrons and their relative concentration with respect to the nuclear concentration. Thus the parameters entering this model are the MW intensity ν_1, a coefficient Λ^{eSD} defining the eSD process and determining the maximum polarization exchange rate between neighboring bins, T_{max}^{eSD}, the relaxation times T_{1e}, T_{2e} and T_{1n} and the $f(\delta\nu_j)$ intensities derived from the normalized EPR lineshape $f(\delta\nu_e)$. In addition the SE is taken into account by adding effective MW irradiation rates on DQ and ZQ transitions to the coupled equations, determined by an effective pseudo-hyperfine coefficient $\overline{A}^\pm$, representing the interaction between the electrons and the nuclei. In these calculations only one type of nucleus is considered. Necessary extensions will be discussed in greater detail later on in this manuscript.

Solving these rate equations results in the electron polarization $P_e(\delta\nu_j; \delta\nu_{excite}, t_{excite})$

of each bin for a fixed MW frequency $\delta\nu_{excite}$. By using the measured rate constants (T_{1e} and T_{1n}) and finding the best fitting parameters (T_{2e}, Λ^{eSD} and $\overline{A}^{\pm}$) it is possible to simulate ELDOR spectra, $E_e^{sim}(\delta\nu_{excite}, t_{excite}; \delta\nu_j)$ that fit the experimental data, $E_e^{exp}(\delta\nu_{excite}, t_{excite}; \delta\nu_{detect})$ for a set of experimental $\delta\nu_{detect} \approx \delta\nu_j$ values. With the same parameters we generate the electron polarization profiles, $P_e(\delta\nu_j; \delta\nu_{excite}, t_{excite})$ for all $\delta\nu_j$ values that form the basis from which the basic DNP lineshapes of the different mechanisms can be derived.

Simulation of the basic SE-DNP, and iCE-DNP spectra

After calculating the steady state polarization profiles, $P_e(\delta\nu_{detect}; \delta\nu_{excite}, t_{excite})$, (for a t_{excite} that is long enough for the electrons to reach a steady state), we can use them to simulate the basic DNP lineshapes of the SE, dCE and iCE.

The MW frequency dependence of the ^{1}H and ^{2}H SE-DNP lineshapes can be obtained by using these profiles and assuming that the nuclear polarization is proportional to the polarizations of the electrons contributing to the SE enhancement taking their relative numbers $f_e(\delta\nu)$ into account [19]:

$$S_{SE}^n(\delta\nu_{excite}) = N_{SE}^{-1}\{f_{e-}P_e(\delta\nu_{excite}-\nu_n; \delta\nu_{excite}, t_{excite}) - f_{e+}P_e(\delta\nu_{excite}+\nu_n; \delta\nu_{excite}, t_{excite})\} \tag{1}$$

where $n =^1$ H or ^{2}H, and the relative intensities $f_{e\pm} = f(\delta\nu_{excite} \pm \nu_n)$ are calculated from the normalized echo detected EPR spectrum that is measured on a sample with a low radical concentration on a W-band spectrometer. N_{SE}^{-1} is a normalization factor for the SE-DNP spectrum $S_{SE}^n(\delta\nu_{excite})$.

The iCE-DNP lineshapes can be calculated by taking into account all pairs of CE electrons and not just the ones that are directly affected by the MW irradiation:

$$S_{iCE}^{^1H}(\delta\nu_{excite}) = N_{iCE-^1H}^{-1} \sum_j f_j f_{j-} \frac{P_e(\delta\nu_j; \delta\nu_{excite}, t_{excite}) - P_e(\delta\nu_j - \nu_{1H}; \delta\nu_{excite}, t_{excite})}{1 - P_e(\delta\nu_j; \delta\nu_{excite}, t_{excite}P_e(\delta\nu_j - \nu_{1H}; \delta\nu_{excite}, t_{excite})} \tag{2}$$

$$S_{iCE}^{^2H}(\delta\nu_{excite}) = N_{iCE-^2H}^{-1} \sum_j f_j f_{j-} \frac{4}{3} \times \frac{P_e(\delta\nu_j; \delta\nu_{excite}, t_{excite}) - P_e(\delta\nu_j - \nu_{2H}; \delta\nu_{excite}, t_{excite})}{1 - P_e(\delta\nu_j; \delta\nu_{excite}, t_{excite}P_e(\delta\nu_j - \nu_{2H}; \delta\nu_{excite}, t_{excite})}$$

where $\delta\nu_j$ is again the frequency of the j bin of the EPR line, the relative intensities of the EPR line, f_j and f_{j-}, are $f(\delta\nu_j)$ and $f(\delta\nu_j - \nu_n)$, respectively, and $N_{iCE-^nH}^{-1}$ are factor that normalize the $S_{iCE}^{nH}(\delta\nu_{excite})$'s. The sum over j represents all pairs of electrons separated by $\delta\nu_n$ (all CE electron pairs) within the whole frequency range of the EPR spectrum. In

this work we do not explicitly calculate the dCE lineshape, as the CE electron pairs that contribute to the dCE are included in the steady state iCE calculation. The constant of $\frac{4}{3}$ is included in order to take into account the fact that ^{2}H nuclei have a spin of S=1. An explanation of the origin of this constant is given in Section 4.2.

2.2.2 Reduced Liouville space simulations

Numerical simulations of the spin dynamics of small systems were performed by evaluating the time evolution of the elements of the spin-density state vector assuming a main interaction Hamiltonian, H_0, with Zeeman, hyperfine and dipolar interaction terms, and a MW irradiation Hamiltonian, H_{MW}. During the calculations only the population elements of the state vector in the diagonalized representation of H_0 are considered and their time evolution under the influence of the relaxation times and the MW irradiation rates are calculated. The method of simulation is described in detail in Ref. [74].

A general Hamiltonian, consisting of several electrons ($e = a, b, c$) and several ^{1}H ($i = 1, ..., N_{^1H}$) and ^{2}H ($j = 1, ..., N_{^2H}$) nuclei can be written, in the MW rotating frame, as follows:

$$H_0 = \sum_e (\delta\nu_e - \delta\nu_{MW})S_{z,e} + \sum_{e,e'} \Delta_{ee'}(2S_{z,e}S_{z,e'} - S_{x,e}S_{x,e'} - S_{y,e}S_{y,e'})$$

$$+ \sum_{e,i,j}[A_{z,eH,i}S_{z,e}H_{z,i} + \frac{1}{2}(A^{\pm}_{eH,i}S_{z,e}H^+_i + A^{\pm}_{eH,i}S_{z,e}H^-_i) + A_{z,eD,j}S_zD_{z,j} + \frac{1}{2}(A^{\pm}_{eD,j}S_{z,e}D^+_j + A^{\pm}_{eC}S_{z,e}D^-_j)]$$

$$\tag{3}$$

$$+ \sum_{i,j}[\nu_{^1H}H_{z,i} + \nu_{^2H}D_{z,j}]$$

where S_p are the electron angular momentum operators with $p = x, y, z$ and $H_{z,i}$, $H^{\pm}_i$, $D_{z,j}$ and $D^{\pm}_j$ are the angular momentum operator components of ^{1}H-nucleus i and ^{2}H-nucleus j. $(\delta\nu_e - \delta\nu_{MW})$ is the electron off-resonance frequency, $A_{z,en,i}$ and $A^{\pm}_{en,i}$ are the secular and pseudo-secular coefficients of the dipolar-hyperfine interactions between electron e and proton i with $n = H$, and similarly for a deuteron j with $n = D$, $\Delta_{ee'}$ is the electron-electron dipolar coupling constant between electrons e and e'. For simplicity we ignored the quadrupolar interactions of the ^{2}H nuclei and the homonuclear and heteronuclear dipolar interactions in the calculations. During MW irradiation we must add to H_0 a MW irradiation term with an irradiation strength ν_1:

$$H_{MW} = 2\pi\nu_1 S_x. \tag{4}$$

The relevant relaxation times added to the calculations are the spin-lattice relaxation times of the electrons, T_{1e}, and of the ^{1}H and ^{2}H nuclei, $T_{1,^1H}$ and $T_{1,^2H}$, respectively, and

in addition the spin-spin relaxation times of the electrons T_{2e} and of the nuclei T_{2n}. When needed, we also consider nuclear spin diffusion, with a nuclear dipolar cross-relaxation time constant T_{1d}^H taking care of the exchange of polarization between the different ^{1}H nuclei, and electron spectral diffusion with an electron cross-relaxation time constant T_{1D} enabling polarization exchange between electrons in the system. In some of the reduced Liouville space simulations, strong spin selective RF pulses are introduced that can cause selective nuclear saturation.

In this work we consider a set of different spin systems, which will be described in Sections. 4.3 and 4.2. In these sections we will discuss (i) the ^{2}H-iCE by calculating the polarizations of a three-spin system containing two interacting electrons a and b coupled to a single ^{2}H nucleus, $\{e_a - e_b - {}^2\text{H}\}$, with $|\delta\nu_a - \delta\nu_b| \approx \nu_{{}^2\text{H}}$, (ii) the hnCE by calculating the polarizations of a six spin system containing again two interacting electrons a and b coupled to three ^{1}H nuclei and to a single ^{2}H nuclei, $\{e_a - e_b - ({}^1\text{H}_3, {}^2\text{H})\}$, with $|\delta\nu_a - \delta\nu_b| \approx \nu_{{}^1\text{H}} \pm \nu_{{}^2\text{H}}$, and (iii) the hnCE by calculating the polarizations of an eight spin system containing the six spin $e_a - e_b - ({}^1\text{H}_3, {}^2\text{H})$ system with the addition of two extra electrons; one for fixing the polarizations of e_a and e_b via cross-relaxation, one for fixing the proton polarization via the ^{1}H-SE-DNP mechanism. The values of the interaction and relaxation parameters used during the various simulations of the polarizations are given in the appropriate figure captions. In all cases the polarizations are defined such that for $T \rightarrow 0$ K they reach the value of 1.

3 Experimental results

3.1 DNP / ELDOR Spectra and their Fits

3.1.1 DNP spectra

To study the ^{1}H-DNP and ^{2}H-DNP processes we performed experiments on the three ("H$_2$O", "D$_2$O" and "fully deuterated") samples. Steady state ^{1}H- and ^{2}H-DNP spectra were acquired at two temperatures, 6 K and 20 K, from each of the three samples (from the "fully deuterated" sample only ^{2}H-DNP was measured). The ^{1}H-DNP and ^{2}H-DNP spectra of the "H$_2$O" sample are presented on Fig. 1a,b and of the "D$_2$O" sample in Fig. 1c,d. The ^{2}H-DNP spectra of the "fully deuterated" sample are shown in Fig. 1e,f . The maximal enhancements obtained for each DNP spectrum are summarized in Table 1.

	"H$_2$O"		"D$_2$O"		"fully deuterated"
	^{1}H enhancements	^{2}H enhancements	^{1}H enhancements	^{2}H enhancements	^{2}H enhancements
6 K	79	92	85	70	172
20 K	81	87	75	106	156

Table 1: Summary of maximum steady state ^{1}H and ^{2}H DNP enhancements.

It is evident from the spectra in Fig. 1 and from Table 1 that all the maximum steady state ^{1}H and ^{2}H enhancements at 6 K and 20 K are rather close in the "H$_2$O" and "D$_2$O" sample, except for the ^{2}H enhancement in the "D$_2$O" sample at 20 K. When comparing the maximum enhancements of the different types of nuclei we must realize that the ^{1}H- and ^{2}H-DNP spectra were acquired in separate experiments with different DNP probes with potentially small differences in their MW field intensities and MW penetration at the sample positions. These differences can be a source of some deviations in the enhancement values. Keeping that in mind, our results thus imply that at steady state conditions the ratios between the maximum ^{1}H and ^{2}H polarizations in the two samples are about equal to the ratio of the gyromagnetic ratios of the two spin types, $\gamma_{^1H}/\gamma_{^2H}$, despite the clear differences between the shapes of the DNP spectra at 20 K.

The enhancements of the "fully deuterated" sample in Fig. 1e and f do not match the values in 1 because these particular ^{2}H-DNP spectra were not measured at the steady state of the DNP enhancement. The lineshape in this case was found to be invariant with irradiation time. The enhancements in the table were obtained from the maximum enhancements measured during DNP buildup experiments performed at the frequencies of maximum enhancement in the DNP spectra.
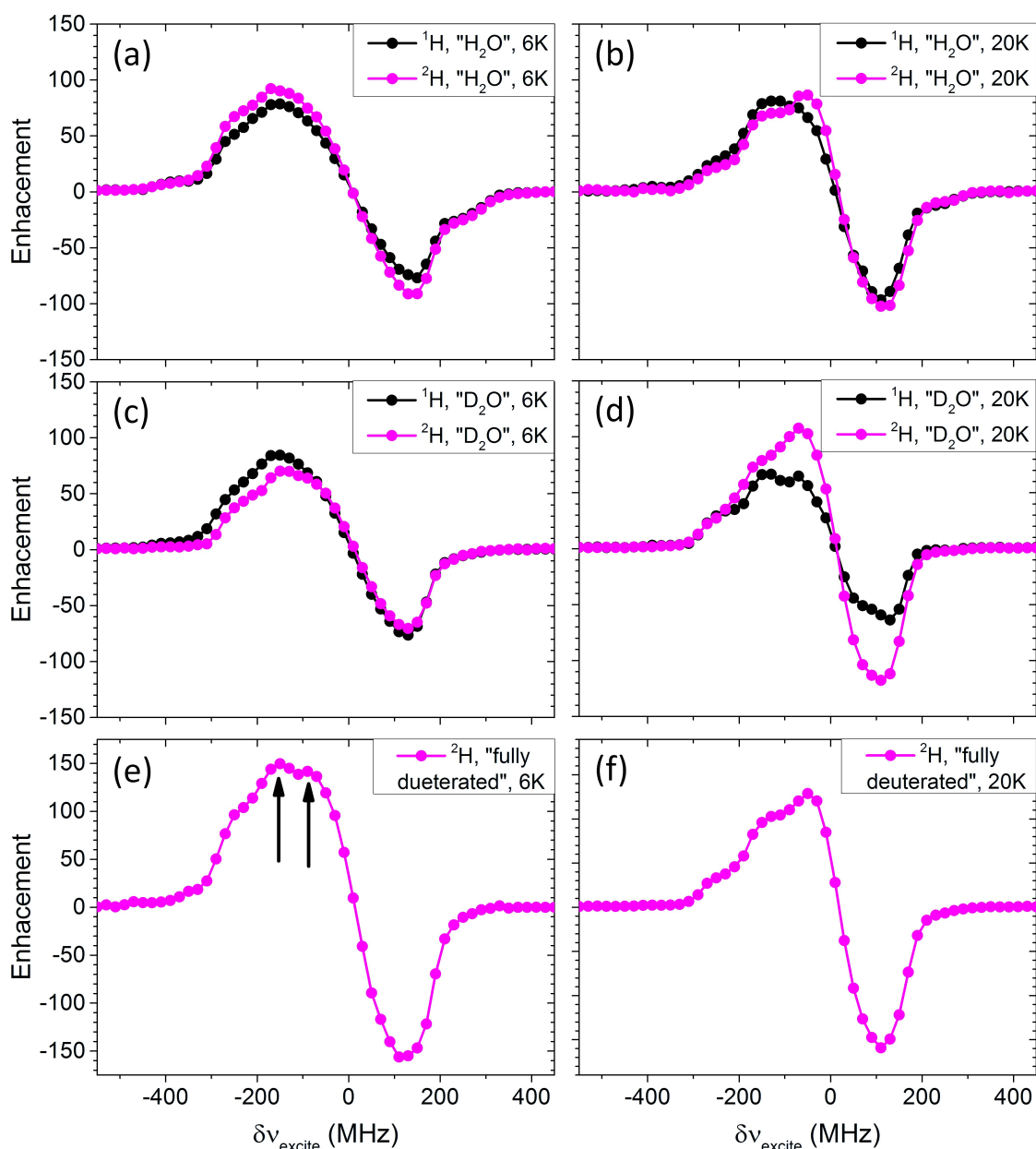
Figure 1: Steady state DNP spectra of ^{1}H (black) and ^{2}H (magenta) nuclei at 6 K (left column) and 20 K (right column) for the "H$_2$O" sample (a and b), "D$_2$O" sample (c and d) and "fully deuterated" sample (e and f). The arrows refer to the double maximum shape of the ^{2}H-DNP spectrum as discussed in the text. The lines connecting the symbols are to guide the eye. The x-axis is plotted with reference to $\nu_{ref} = 95$ GHz.

When we compare the 6 K spectra (Fig. 1 a, c, e) to the 20 K spectra (Fig. 1 b, d, f) for all three samples, we observe that the steady state DNP lineshapes of each nucleus (^{1}H-DNP spectra in black and ^{2}H-DNP in magenta) change as a function of temperature. The ^{1}H-DNP spectra as a function of temperature show a slight narrowing of the overall spectrum and a smaller separation between the positive and negative enhancement peaks. Going from 6 K to 20 K the ^{2}H-DNP spectrum becomes more asymmetric, with three

frequency steps at the low frequency side. We should mention here that the [1]H-DNP spectra at 6 K and 20 K of the "H_2O" sample are very similar to the spectra of the fully protonated 50% H_2O / DMSO sample as reported in Refs. [19, 59].

To compare the DNP spectral lineshapes of the same nucleus obtained from the "H_2O" and "D_2O" samples we draw their normalized spectra, already shown in Fig. 1, in Fig. 2. Here the ^{1}H spectra of the two samples as well as their ^{2}H spectra at 6 and 20 K are overlaid. At first we see that the lineshapes of the ^{1}H spectra of the two samples at both temperatures are rather similar. The main differences are the intensities of the spectra in the areas outside the EPR line, which are marked in gray for $\delta\nu_{excite} > 200 MHz$ and $\delta\nu_{excite} < -300 MHz$. These intensities above 200 MHz are somewhat larger in the "H_2O" sample than the "D_2O" sample. Other small differences are the shapes above ~150 MHz, while the spectral features below this value are almost the same. The comparison between the [2]H-DNP lineshapes from the "H_2O" and "D_2O" samples at 20 K shows that they are almost identical to one another and that they exhibit the same features as the spectrum from the "fully deuterated" sample in Fig. 1f. In the SI we demonstrate that the [2]H-DNP spectrum of "H_2O" at 40 K shows again the same features. At 6 K, however, the [2]H-DNP profiles of the "H_2O" and "D_2O" samples are really different from that of the "fully deuterated" sample in Fig. 2e, namely the double maximum in the "fully deuterated" sample is missing in the "H_2O" spectrum and hardly observable in the "D_2O" spectrum (Fig. 2c). An additional difference between the "H_2O" and "D_2O" spectra at 6 K is their intensities outside the EPR line, where above 200 MHz the "H_2O" intensity is somewhat larger than the "D_2O" intensity. This same differences can be seen also, but to a lesser extent, when comparing the "H_2O" and "D_2O" spectra at 20 K.

The enhancement outside of the EPR line is related to the [1]H-SE contribution to the electron depolarization and thus to the iCE-DNP spectra, as explained in some detail in Section 3.1.2. It is known that water can form hydrogen bonds with nitroxide radicals [75] and subsequently the protonated water molecules in the "H_2O" sample can have a large ^{1}H hyperfine interaction and thus can result in a significant SE enhancement outside the EPR line. In the case of the deuterated water in the "D_2O" sample the hyperfine interaction with the nearest protons, on the DMSO molecules, is much smaller and consequently the ^{1}H spectra of "D_2O" have a smaller [1]H-SE enhancement outside the EPR line than of the "H_2O" sample.
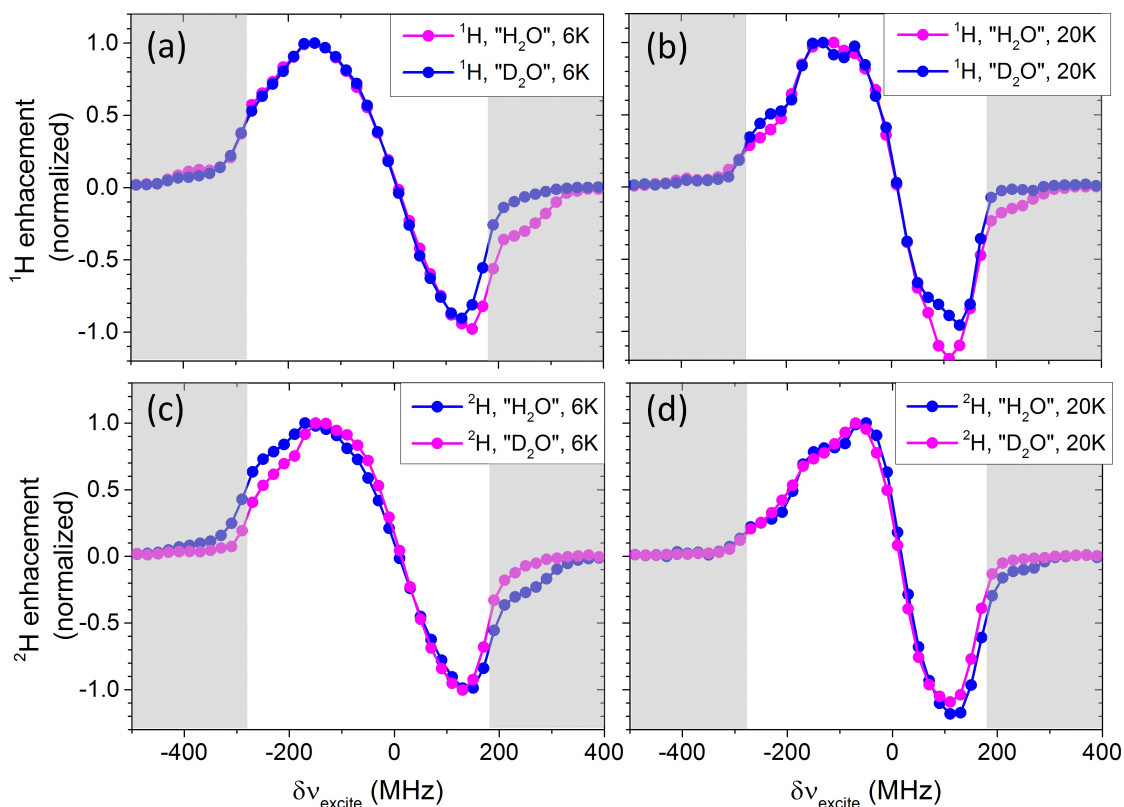
Figure 2: Comparison of the normalized DNP spectra of the "H$_2$O" (blue) and "D$_2$O" (magenta) samples for (a) ^{1}H at 6 K, (b) ^{1}H at 20 K, (c) ^{2}H at 6 K and (d) ^{2}H at 20 K. The gray areas refer to the sections of the DNP spectra outside of the span of the EPR spectrum. The lines connecting the symbols are to guide the eye. The x-axis is plotted with reference to $\nu_{ref} = 95$ GHz.

Finally, we compare the ^{1}H and ^{2}H-DNP spectra for each sample at the two measured temperatures. It is clear from Figs. 1b and d that the shapes of the ^{1}H and ^{2}H-DNP spectra are different at 20 K. However, from Figs. 1a and c it is clear that at 6 K their shapes are very similar. In order to demonstrate this similarity we re-plot these spectra after normalization in Fig. 3. From the normalized spectra it is clear that the ^{1}H and ^{2}H-DNP spectra at 6 K of the "H$_2$O" sample have identical shapes, and that the spectra of the "D$_2$O" sample have very similar shapes. Because the shape and the intensity (measured difference of only 15%) of the ^{2}H-DNP spectrum at 6 K are identical to those of the ^{1}H-DNP spectrum, and because their shapes are different than the "fully deuterated" spectrum at that temperature (see Fig. 1e), we measured the ^{2}H-DNP spectrum of the "H$_2$O" sample as a function of MW irradiation time t_{excite} to explore the evolution of the ^{2}H-DNP lineshape. As expected the ^{2}H-DNP enhancement grows as a function of MW irradiation time as shown in Fig. 4a. However, when we compare the normalized ^{2}H-DNP spectrum after t_{excite}=1 sec with the normalized steady state spectrum we see in Fig. 4b that their shapes differ. In fact, the ^{2}H-DNP spectrum after t_{excite}= 1 sec has the same

double maximum (see arrows in Fig. 4b) as in the "fully deuterated" spectrum at 6 K, but the steady state shape does not. This result suggests that the ^{2}H-DNP lineshape starts out looking like a real ^{2}H-DNP spectrum, but then as t_{excite} is extended the shape changes until it becomes identical to the shape of the ^{1}H-DNP spectrum. Thus the shape of the ^{2}H-DNP spectrum starts out as a shape corresponding to a direct electron-deuterium DNP polarization, and for prolonged irradiation times changes to get the shape corresponding to an electron-proton DNP mechanism. The ^{1}H-DNP and ^{2}H-DNP spectra of the "D$_2$O" sample become also very similar, as can be seen in Fig. 3b. These results indicate that there exists some "cross-talk" between the two nuclei, such that at steady state the ^{1}H polarization somehow determines the value of the ^{2}H polarization.
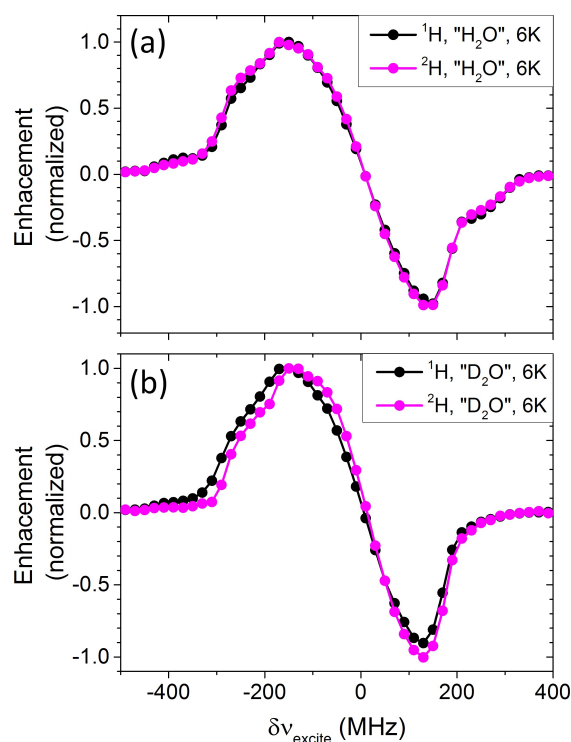
Figure 3: Comparison of the normalized steady state DNP spectra of ^{1}H (black) and ^{2}H (magenta) nuclei for (a) the "H$_2$O" spectra at 6 K, (b) the "D$_2$O" spectra at 6 K. The lines connecting the symbols are to guide the eye. The x-axis is plotted with reference to $\nu_{ref} = 95$ GHz.

15
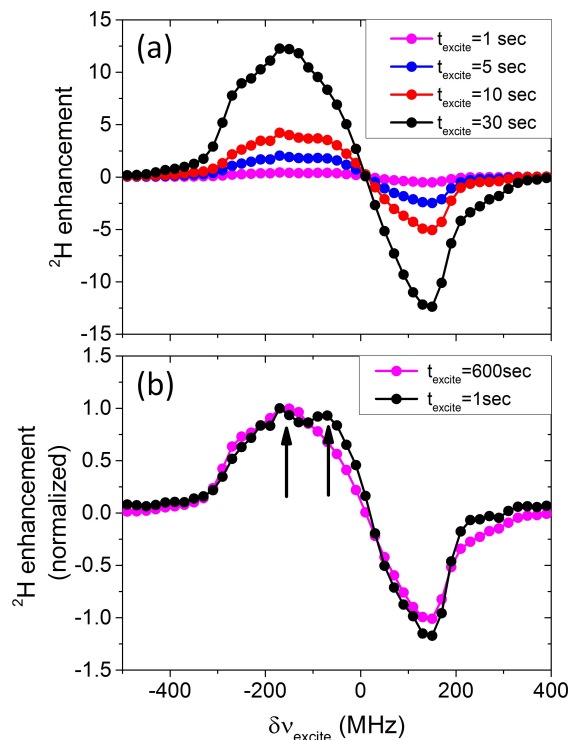
Figure 4: (a) DNP spectra of the ^{2}H nuclei at 6 K measured at different values of t_{excite}. (b) Comparison of the normalized DNP spectra lineshapes at the steady state (magenta) and short $t_{excite} = 1$ sec (black). The arrows in (b) refer to the double maximum shape of the ^{2}H-DNP spectrum as discussed in the text. The lines connecting the symbols are to guide the eye. The x-axis is plotted with reference to $\nu_{ref} = 95$ GHz.

3.1.2 ELDOR spectra and their simulated fits

In order to get a better understanding of the DNP mechanisms leading to the DNP spectra described in Section 3.1.1, we use our theoretical DNP models to analyze the experimental DNP spectra. As a first requirement to do so we must construct the frequency dependent electron polarization profiles along the whole inhomogeneously broadened EPR line, which are a result of a prolonged MW irradiation at different frequencies $\delta\nu_{excite}$. These polarization distributions are derived from ELDOR experiments, as described in detail in Refs. [19, 23] and summarized in the Simulation Methods section.

In practice these ELDOR experiments are performed by choosing a fixed echo detection frequency $\delta\nu_{detect}$ and by recording echo amplitudes $S(\delta\nu_{excite}, t_{excite}; \delta\nu_{detect})$ as a function of the frequency $\delta\nu_{excite}$ and the duration t_{excite} of a MW excitation pulse. Each such experimental data-set is normalized, with respect to the echo amplitudes $S_{ref}(\delta\nu_{detect})$ obtained with $\delta\nu_{excite}$ placed far from the frequency span of the EPR line, to obtain normalized experimental DNP spectra:

$$E_e^{exp}(\delta\nu_{excite}, t_{excite}; \delta\nu_{detect}) = \frac{S(\delta\nu_{excite}, t_{excite}; \delta\nu_{detect})}{S_{ref}(\delta\nu_{detect})}.$$

Subsets of these ELDOR spectra measured on the "H_2O" sample at 6 K and 20 K are presented in Figs. 7 and 6, respectively, by black symbols. The rest of the measured ELDOR spectra are presented in Figs. S2 and S3 of the SI. The detection frequencies of the different spectra, $\delta\nu_{detect}$, are marked in the figure with small arrows. Some spectra show pronounced minima at the center position of the EPR line in addition to the sharp minima at $\delta\nu_{excite} = \delta\nu_{detect}$. The minima when $\delta\nu_{excite} = \delta\nu_{detect}$ are due to direct on-resonance irradiation on the electrons, while the minima at the center of the EPR line are the result of strong eSD processes, as explicitly explained in Ref. [23]. At 20 K (Fig. 6) the ELDOR spectra are narrower than at 6 K (Fig. 7), which is likely a result of the shorter T_{1e} values that diminish the MW saturation effect and presumably limits the effect of the eSD process. It is worth noting that these ELDOR spectra are virtually indistinguishable from the ones obtained from a fully protonated sample under the same conditions, as reported by Hovav et. al [23].
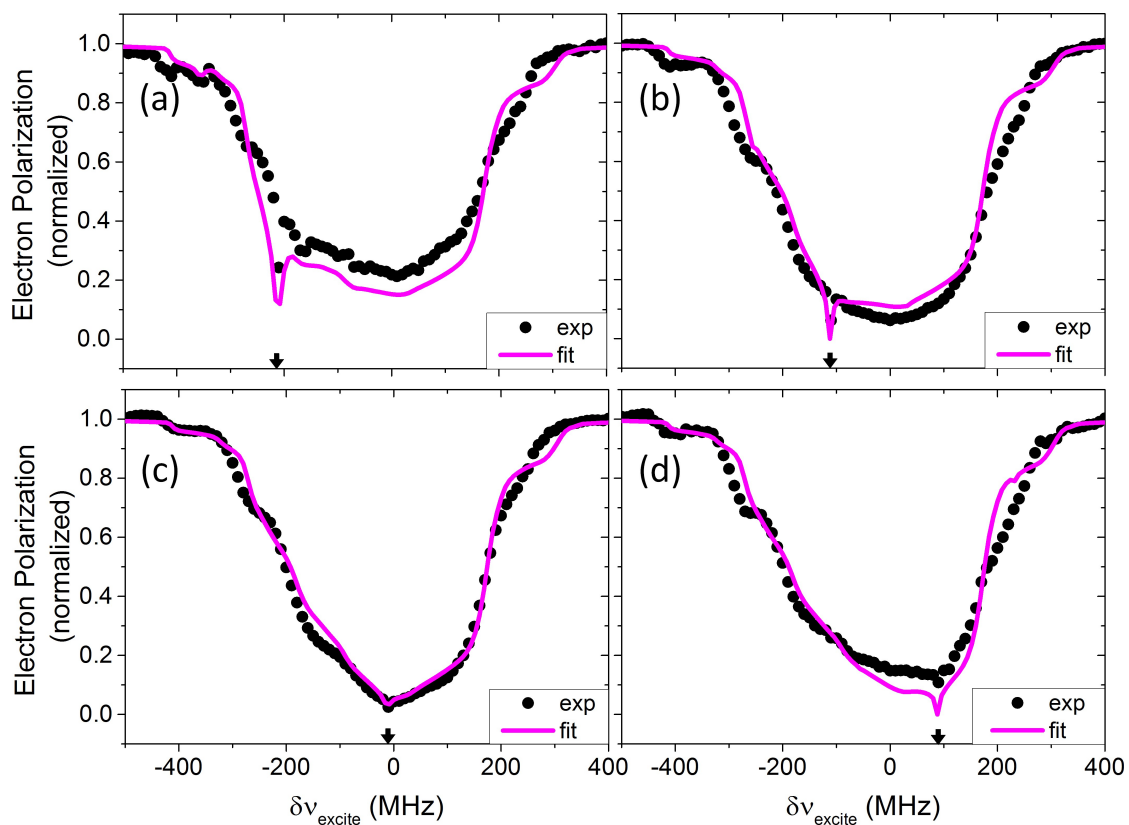
Figure 5: Experimental ELDOR spectra measured at 6 K on the "H$_2$O" sample (black symbols) overlaid with the simulated ELDOR spectra (magenta lines). The detection frequencies are marked by the small black arrows: (a) $\delta\nu_{detect}$ =-210 MHz, (b) $\delta\nu_{detect}$ =-110 MHz, (c) $\delta\nu_{detect}$ =-1 MHz and (d) $\delta\nu_{detect}$ =-90 MHz. The parameters for the simulations are given in Table 2. The x-axis is plotted with reference to ν_{ref} = 95 GHz.
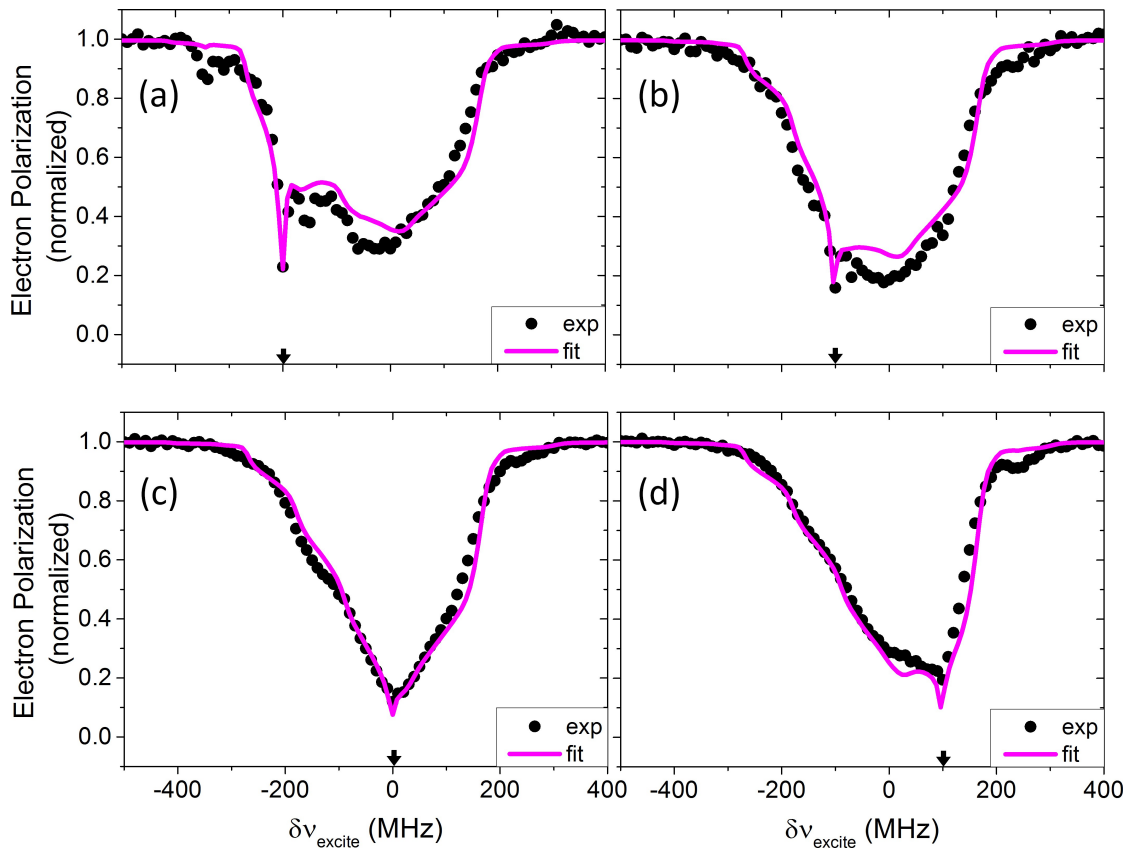
Figure 6: Experimental ELDOR spectra measured at 20 K on the "H_2O" sample (black symbols) overlaid with the simulated ELDOR spectra (magenta lines). The detection frequencies are marked by the small black arrows: (a) $\delta\nu_{detect}$ =-200 MHz, (b) $\delta\nu_{detect}$ =-100 MHz, (c) $\delta\nu_{detect}$ =0 MHz and (d) $\delta\nu_{detect}$ =-100 MHz. The parameters for the simulations are given in Table 2. The x-axis is plotted with reference to ν_{ref} = 95 GHz.

The ELDOR spectra were fitted using the model introduced by Hovav et. al. [19, 23] by changing the three free parameters, T_{2e}, $\overline{A}^{\pm}$ and Λ^{eSD}, during the simulations and fixing the the rest of the input parameters close to their measured experimental values. The three parameters were changed systematically to find the best simultaneous fit to all the measured ELDOR spectra at each temperature. The quality of the simultaneous fits to all the ELDOR spectra was estimated by the parameter σ_{ELDORS} defined as

$$\sigma_{ELDORS} = \sqrt{\frac{\sum_{\delta\nu_{excite}} \sum_{\delta\nu_{detect}} [E_e^{exp}(\nu_{excite}, \nu_{detect}) - E_e^{sim}(\nu_{excite}, \nu_{detect})]^2}{n_{\delta\nu_{excite}} n_{\delta\nu_{detect}}}}$$

where $E_e^{sim}(\delta\nu_{excite}, \delta\nu_{detect})$ denotes the simulated normalized ELDOR spectra for a given set of $\delta\nu_{excite}$ and $\delta\nu_{detect}$ values; $n_{\delta\nu_{excite}}$ and $n_{\delta\nu_{detect}}$ are the total number of data points measured as a function of $\delta\nu_{excite}$ and of $\delta\nu_{detect}$, respectively. As will be discussed in Section 3.1.3 for each combination of the parameters $\overline{A}^{\pm}$, Λ^{eSD} and T_{2e} a normalized

DNP lineshape was also simulated and the quality of fit parameter σ_{DNP} was calculated by considering the experimental lineshape.
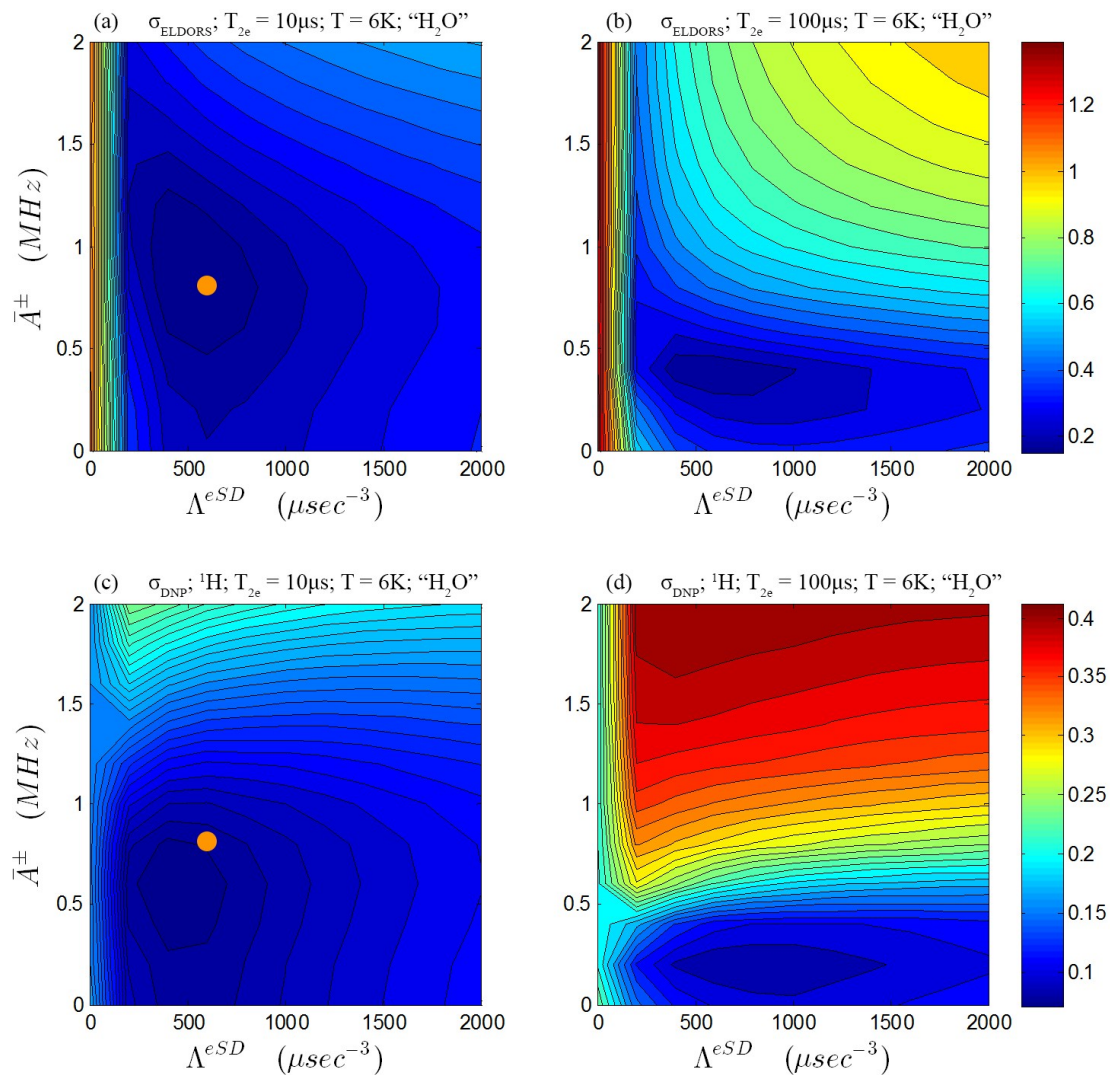
Figure 7: Qualityof fit parameter σ_{ELDORS}, of the simultaneous fitting of the 9 experimental ELDOR spectra measured at 6 K on the "H_2O" sample, plotted against $\overline{A}^{\pm}$ and Λ^{eSD} for (a) $T_{2e} = 10\mu s$ and (b) $T_{2e} = 100\mu s$. Quality of fit parameter σ_{DNP}o f the simulated ^{1}H-DNP spectrum with respect to the normalized ^{1}H-DNP spectrum measured at 6 K on the "H_2O" sample, plotted again against $\overline{A}^{\pm}$ and Λ^{eSD} for (c) $T_{2e} = 10\mu s$ and (d) $T_{2e} = 100\mu s$. The orange dot marks the values of $\overline{A}^{\pm}$ and, Λ^{eSD} and T_{2e} used for the final ELDOR analysis, as listed in table 2. The rest of the parameters used for simulations are listed in table 2 as well.
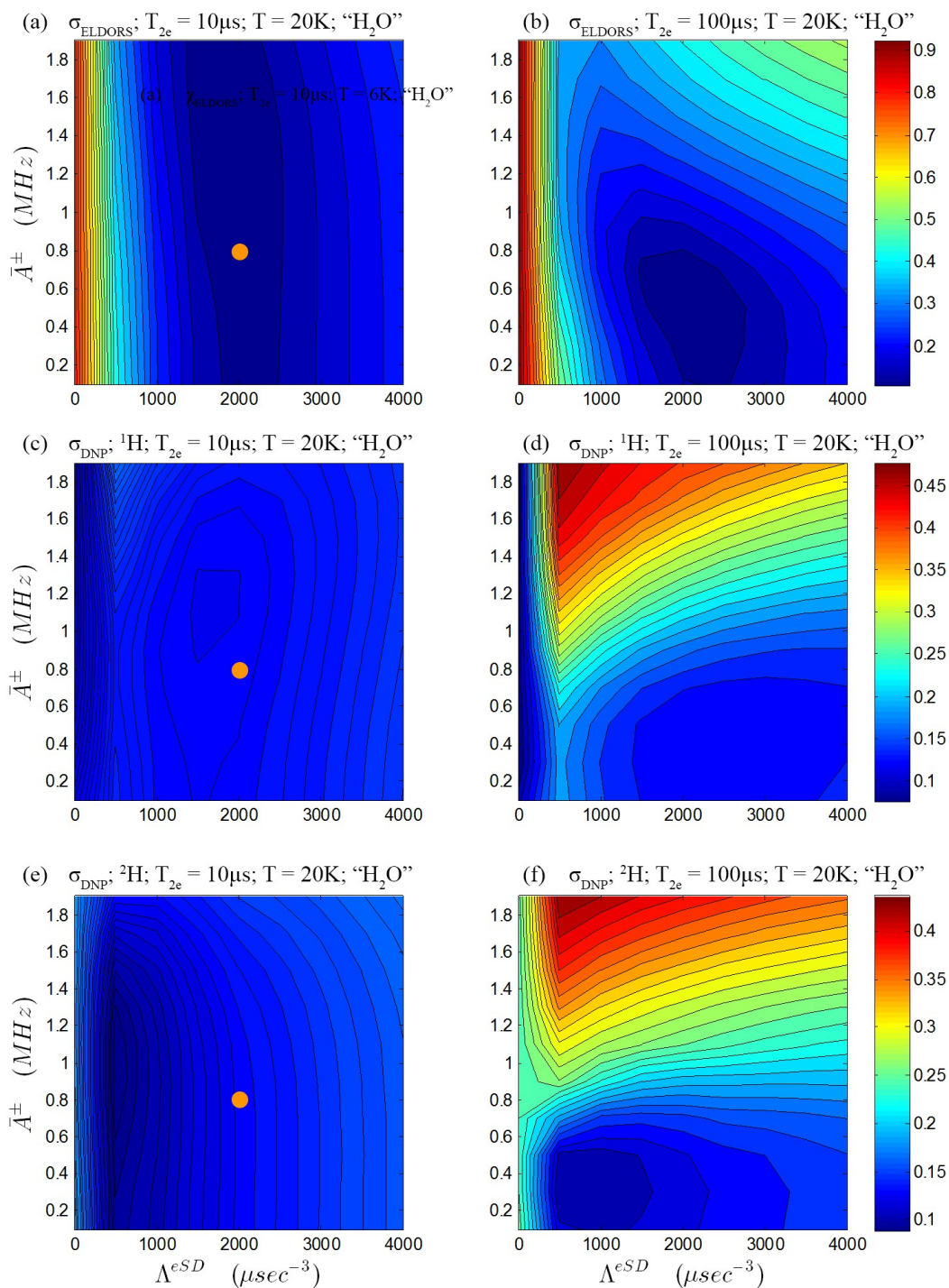
Figure 8: Quality of fit parameter σ_{ELDORS} of the simultaneous fitting of the 7 experimental ELDOR spectra measured at 20 K on the "H_2O" sample, plotted against $\overline{A}^{\pm}$ and Λ^{eSD} for (a) $T_{2e} = 10\mu s$ and (b) $T_{2e} = 100\mu s$. Quality of fit parameter σ_{DNP} of the simulated ^{1}H-DNP spectrum with respect to the normalized ^{1}H-DNP spectrum measured at 6 K on the "H_2O" sample, plotted again against $\overline{A}^{\pm}$ and Λ^{eSD} for (c) $T_{2e} = 10\mu s$ and (d) $T_{2e} = 100\mu s$. Quality of fit parameter σ_{DNP} of the simulated ^{2}H-DNP spectrum with respect to the normalized ^{2}H-DNP spectrum measured at at 20 K for the "H_2O" sample, plotted against $\overline{A}^{\pm}$ and Λ^{eSD} for (e) $T_{2e} = 10\mu s$ and (f) $T_{2e} = 100\mu s$. The orange dot marks the values of $\overline{A}^{\pm}$ and, Λ^{eSD} and T_{2e} used for the final ELDOR analysis, as listed in table 2. The rest of the parameters used for simulations are listed in table 2 as well.

Similar to our previous findings, different combinations of the values of T_{2e} and $\overline{A}^{\pm}$ (see supporting information in Ref. [79]) can result in equally good agreements between the simulated and experimental spectra. An example of this can be seen in Fig. 7, where χ_{ELDORS} for the ELDOR spectra aquired at 6 K is plotted versus $\overline{A}^{\pm}$ and Λ^{eSD} for $T_{2e} = 10\mu s$ and $T_{2e} = 100\mu s$ in (a) and (b), respectively. In both 2D plots a clear minimum is present, with almost the same value of σ_{ELDORS}. Similar minima are obtained for other T_{2e} values (data not shown). Because the simulated profiles of the DNP spectra depend only on the shapes of the best-fitted calculated electron polarization profiles and not on the underlying parameters used to calculate them, the exact choice of the parameters becomes unimportant for simulation of the DNP spectra, as is detailed in Section 3.1.1. In analogy 2D plots of σ_{ELDORS} as a function of $\overline{A}^{\pm}$ and Λ^{eSD} for the ELDOR spectra measured at 20 K are shown in Fig. 6a and b for $T_{2e} = 10\mu s$ and $T_{2e} = 100\mu s$, respectively.

A comparison between the parameters resulting in a good fit for 6 K and 20 K data reveals that for a given value of T_{2e} the best fit to the ELDOR spectra is obtained for a Λ^{eSD} value that is higher at 20 K than at 6 K, meaning an increased strength of the eSD rate at higher temperature. For both 20 K and 6 K data, the choice of the higher T_{2e} value equal to $100\mu s$ resulted in samller $\overline{A}^{\pm}$ values. Since the latter represents the strength of the electron-proton interaction and is not expected to change with temperature, we decided to keep it constant at 0.8 MHz (the value for 6 K) and fix the T_{2e} value at $10\mu s$. Consquently, the change in parameters as function of temperature is then limited to the measured values of T_{1e} and $T_{1,^{1}\mathrm{H}}$ and the fitting parameter Λ^{eSD}. The parameters chosen for the subsequent simulations of the DNP spectra are depicted as orange dots in Fig. 7 and Fig. 8 and are summurized in Table 2. Because the MW irradiation time was much shorter than $T_{1,^{1}\mathrm{H}}$, changing $T_{1,^{1}\mathrm{H}}$ did not have an effect on the simulated ELDOR spectra. We note that during the fitting procedure it was not necessary to take the presence of the ^{2}H nuclei in the sample into account. This is also consistent with the observation that the ELDOR spectra measured for this work are very similar to the ones previously published for a fully protonated sample under the same conditions [23].

Overlay of the experimental and simulated ELDOR spectra for the parametes listed in table 2.are shown in Figs. 5 and6 for the data measured at 6 K and 20 K, respectively, as magenta lines. As revealed also by the χ_{ELDORS} plots, we achieved a good agreement between all the experimental ELDOR spectra and the simulations, with the main discrepancies showing up in the region around $\delta\nu_{excite} = 250$ MHz. Possible sources of these deviations can be small variations in the EPR line shape as a function of temperature, small MW amplitude changes as a function of $\delta\nu_{detect}$ and/or a possible anisotropy of electron relaxation rates.

Physical Chemistry Chemical Physics Accepted Manuscript

sample	T (K)	T_{1e} (msec)	$T_{1,^1H}$ (sec)	$T_{2e}(\mu sec)$	$\overline{A}^{\pm}$ (MHz)	$\Lambda^{eSD}(\mu sec^{-3})$	T_{max}^{eSD} (msec)
"H₂O"	6	60	30	10	0.8	600	0.031
"H₂O"	20	5.5	13	10	0.8	2000	0.009

Table 2: Parameters used in order to simulate the ELDOR spectra shown in magenta in Figs. 7 and 6. T_{1e} and $T_{1,^1H}$ were measured and T_{2e}, $\overline{A}^{\pm}$ and Λ^{eSD} were fitting parameters. T_{max}^{eSD} was calculated from Λ^{eSD} in order to facilitate comparison between the eSD timescale and T_{1e}. In these simulations only ^1H nuclei were considered. A MW irradiation strength of of $\delta\nu_1 = 0.6$ MHz was used in all the calculations.

ELDOR spectra of the "D₂O" sample were not measured. However we simulated ELDOR spectra using the exact parameters used for the "H₂O" sample but reducing the effective $\overline{A}^{\pm}$ by a factor of 2. These simulated ELDOR spectra are shown in the SI. The $\overline{A}^{\pm}$ parameter represents the effective electron-proton interaction that determines the strength of the effective irradiation on the DQ and ZQ transitions. We should expect that $\overline{A}^{\pm}$ is indeed larger in the "H₂O" than in the "D₂O" sample, since in the latter there are no local ^1H_2O protons that can form hydrogen bonds with the nitroxide radicals. Comparing the "H₂O" ELDOR spectra with the simulated "D₂O" ELDOR spectra in the SI reveals that lowering $\overline{A}^{\pm}$ results only in a slight narrowing of the ELDOR spectra, while leaving the overall shapes similar. The largest difference appears outside of the EPR lines ($\delta\nu_{excite} > 200$ MHz, or $\delta\nu_{excite} < -300$ MHz), at the positions of the ^1H-SE, where there is less depolarization in the simulated spectra than in the "H₂O" ELDOR spectra. The validity of this assumption is confirmed by obtaining a good fit to the DNP spectra of the "D₂O" sample as discussed in more detail in Section 3.1.3.

For the interpretation of the DNP experiments we must determine the shapes of the normalized electron polarization profiles $P_e(\delta\nu_{detect}; \delta\nu_{excite}, t_{excite})$ along the EPR line after a prolonged t_{excite} irradiation period. Such profiles for each $\delta\nu_{excite}$ value are constructed by using the parameters obtained from the fit of the ELDOR spectra, $E_e^{exp}(\delta\nu_{excite}, t_{excite}; \delta\nu_{detect})$.

3.1.3 DNP spectra and their fits

Using the simulated electron polarization profiles (the parameters marked by the orange dots in Figs. 7 and 8), it is now possible to simulate basic lineshapes of the SE-DNP and the iCE-DNP spectra. For simplicity, we only compare the basic iCE-DNP shapes to our experimental DNP spectra. The resulting fits of the "H₂O" sample are shown in Fig. 9 and of the "D₂O" sample are shown in the SI. In order to fit the spectra of the "D₂O" sample we used the simulated ELDOR spectra that also appear in the SI. Most spectral features are reproduced, including the enhancements found outside the EPR line originating from the ^1H-SE-DNP mechanism that influences the iCE-DNP lineshape.

For the ^{1}H-DNP spectra acquired at 6 K the agreement of our model with the experiment is rather good for both "H$_2$O" and "D$_2$O" samples. At 20 K the agreement between simulations and experiment for the ^{1}H data is also satisfactory, albeit there is a discrepancy in the negative lobe around +110MHz where the simulations predicts higher negative enhancement than was observed experimentally. We note that the model correctly predicts the overall changes that occur in the ^{1}H lineshapes when increasing the temperature from 6 K to 20 K, such as overall narrowing of the spectra and the positions of all the spectral features observed experimentally. However, the peaks at -150MHz and -75MHz that are very well resolved in ^{1}H-DNP spectra of the "D$_2$O" are less resolved in the simulation. These discrepancies are probably a consequence of imperfections in the simulated electron polarization profiles.

The overall shape and width of the ^{2}H-DNP spectra at both temperatures are well reproduced by the simulations, but there are quite a few discrepancies in the fine structure of the spectra. A main discrepancy is the fact that the simulated ^{2}H-DNP spectrum of the "H$_2$O" sample at 6 K does not match the steady state experimental ^{2}H-DNP spectrum measured after 600 sec. This is not surprising when we realize as shown above that this experimental spectrum is identical to the ^{1}H-DNP spectrum. In contrast, the ^{2}H-DNP spectrum of the "H$_2$O" sample at 6 K measured after t_{excite} = 1 sec (Fig. 10) does agree with most of the features of the simulated ^{2}H-DNP spectrum and despite the mismatch in intensity around 225 MHz present in both, resulting in a smaller value of $\chi_{DNP} = 0.016$, as opposed to $\chi_{DNP} = 0.02$ for the steady state ^{2}H-DNP spectrum. This strongly suggests that at short timescales the polarization of the ^{2}H nuclei is governed by the ^{2}H-iCE mechanism but that for longer timescales the ^{2}H-DNP enhancement is governed by the proton polarization.

Other discrepancies appearing for both the "H$_2$O" and "D$_2$O" samples are the significant overestimation of the simulated enhancement at 175 MHz for the ^{2}H-DNP spectrum. The origin of this overestimation is not known, but we must realize that the ^{2}H lineshape becomes intrinsically more sensitive to the small imperfections in the simulated electron polarization profile than the ^{1}H lineshape due to the nature of the simulation, which considers differences in electron polarizations spaced 22 MHz apart in case of ^{2}H-DNP and 144 MHz apart for ^{1}H-DNP. Other possible sources for the observed discrepancies between simulated and experimental spectra may be that the EPR lineshape used in the simulation was measured at a sample with less than 1 mM TEMPOL concentration or the presence of possible inhomogeneities in the T_{1e} relaxation or spectral diffusion rates within the EPR line.
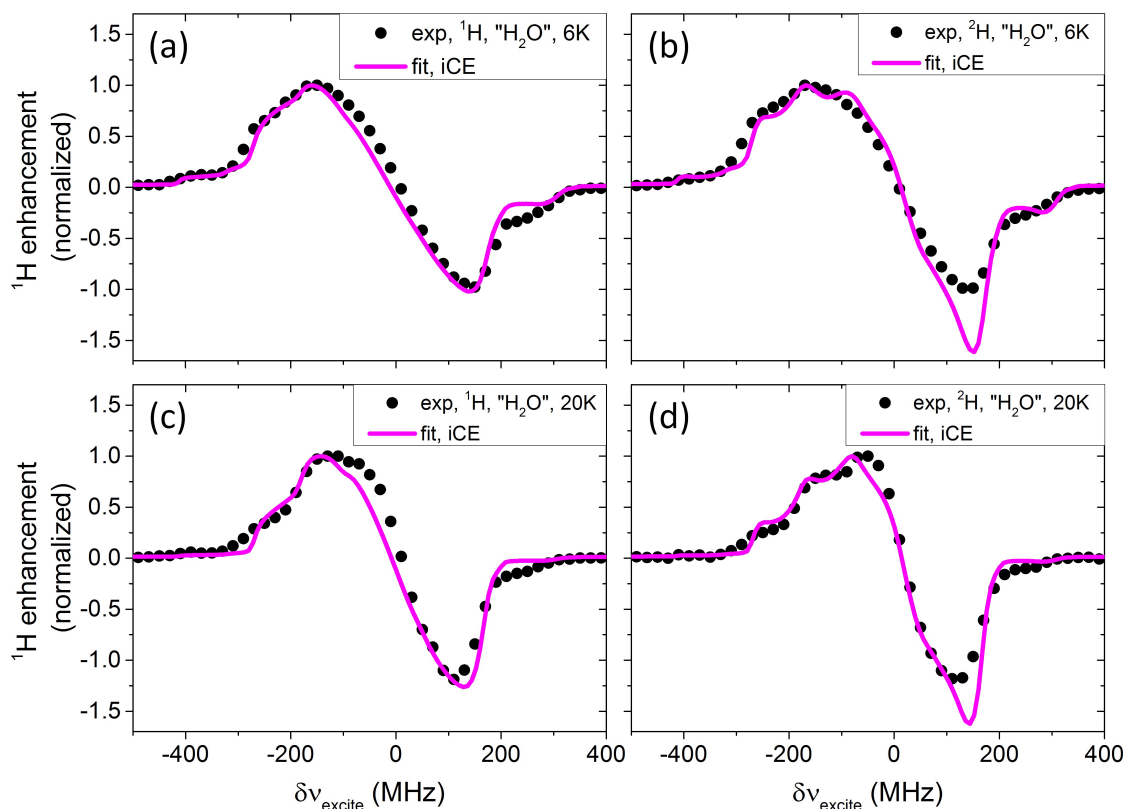
Figure 9: Steady state experimental ^{1}H-DNP spectra (a and c, black symbols) and ^{2}H-DNP spectra (b and d, black symbols) measured on the "H_2O" sample at (a-b) 6 K and (c-d) 20 K. The experimental spectra are overlaid with the simulated iCE-DNP spectra of the appropriate nucleus (magenta lines). The parameters for the simulations are given in Table 2. The x-axis is plotted with reference to $\nu_{ref} = 95$ GHz.
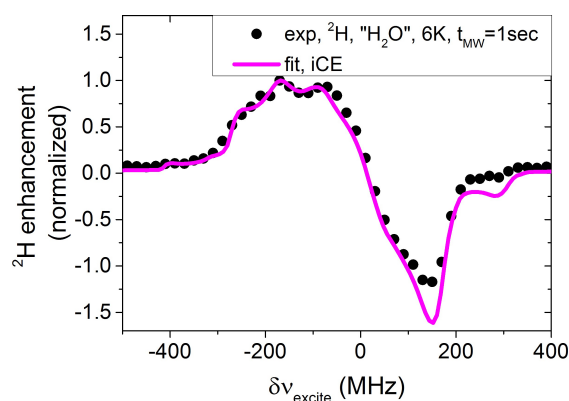
Figure 10: Experimental ^{2}H-DNP spectrum measured on the "H_2O" sample at 6 K with $t_{excite} = 1$ sec (black symbols) overlaid with the simulated ^{2}H-iCE-DNP spectrum (magenta lines). The parameters for the simulations are given in Table 2. The x-axis is plotted with reference to $\nu_{ref} = 95$ GHz.

Although we are at this stage unable to simulate DNP spectra with actual values for their enhancements, we can compare the intensities of the simulated iCE-DNP for the ^{1}H and ^{2}H nuclei. In the experiments the enhancements of the two were similar at a given temperature. This is also true in the simulations, where at 6 K there is only approximately an 18% difference in maximal intensities, and even less at 20 K. This shows that though our current model cannot predict identical ^{1}H and ^{2}H DNP spectra and enhancements, it is able to predict a ratio between the polarizations that is about equal to the ratio of the gyromagnetic ratios of the two spin types $\gamma_{^1H}/\gamma_{^2H}$ similar to experimental observations.

In an analog to the fitting of the ELDOR spectra, we would like to see how changing the ELDOR fitting parameters affects the quality of the DNP fits. We define a paramater for the quality of the fitting of the experimental ^{1}H-DNP spectrum as

$$\sigma_{DNP} = \sqrt{\frac{\sum_{\delta\nu_{excite}}[S^{exp}(\delta\nu_{excite}) - S^{sim}(\delta\nu_{excite})]^2}{n_{\delta\nu_{excite}}}}$$

and is for 6K plotted in Fig. 7 c and d against the same set of parameters (Λ^{eSD} and $\overline{A}^{\pm}$) used to simulate the corresponding ELDOR spectra for $T_{2e} = 10\mu s$ and $T_{2e} = 100\mu s$ respectively. S^{exp} and S^{sim} are the experimental and simulated values, respectively, for the signal intensities in normalzied DNP spectra for given $\delta\nu_{excite}$; $n_{\delta\nu_{excite}}$ is the number of measured points in the DNP spectrum. Similar plots for the fits generated for the ^{1}H-DNP spectrum measured at 20K are presented in Fig. 8c and d for $T_{2e} = 10\mu s$ and $T_{2e} = 100\mu s$, respectively, and for the ^{2}H-DNP spectrum measured at the same temperature in Fig. 8e and f. It is evident that the parameters that result in a good fit of the experimental ELDOR spectra also result in a good overall fit to their corresponding ^{1}H-DNP spectrum. The 2D plots reveal that good agreements between the simualted and experimental DNP spectra can be obtained for a rather large range of Λ^{eSD} and $\overline{A}^{\pm}$ values for $T_{2e} = 10\mu s$. However as we mentioned above the choice of parameters is determined by the fitting procedure of the ELDOR spectra and the good agreement between the simulated and experimental DNP spectra is a confirmation of the validity of the iCE model. Qualitatively similar results are obtained during the analysis of the 20 K ^{2}H-DNP spectrum, though the optimum parameter values are shifted towards higher Λ^{eSD} values (not shown). This is a consequence of the artifact at $\delta\nu_{excite} = +175MHz$ present in the simulations as discussed in more detail below. We did not calculaty the quality of fit for the 6K ^{2}H-DNP spectrum since it is identical to the ^{1}H-DNP spectrum at 6K, something the iCE model can not reproduce.

3.2 Time Dependent Phenomena

In order to further investigate the nature of the similarity between the ^{1}H-DNP and ^{2}H-DNP spectra of the "H$_2$O" sample at 6 K, and their difference at 20 K, we now report

on some temporal characteristics of the buildup, decay and "cross-talk" of the nuclear polarizations.

3.2.1 Saturation recovery and DNP buildup times

As a first step towards characterizing the "H_2O" sample at 6 K we measured the spin-lattice relaxation times of the electrons, T_{1e}, and of the ^1H and ^2H nuclei, $T_{1,^1H}$ and $T_{1,^2H}$ respectively. Next we compared the ^1H- and ^2H-DNP buildup times, $T_{bu,^1H}$ and $T_{bu,^2H}$, and the decay times, $T_{dec,^1H}$ and $T_{dec,^2H}$, of the nuclei after their polarization enhancement. These relaxations, buildup and decay times of the "H_2O" sample are summarized in Table 3.

As expected the electron and nuclear relaxation times at 6 K are longer than at 20 K. We also see that within each temperature, the buildup times are faster than the nuclear spin lattice relaxations, except at 20 K where $T_{bu,^2H} \approx T_{1,^2H}$. The values of $T_{dec,^1H}$ do not depend on the length t_{excite} of the MW irradiation and are shorter than $T_{1,^1H}$. Somewhat unexpectedly, the values of $T_{dec,^2H}$ depend on the length t_{excite}, though also here they are shorter than $T_{1,^2H}$. All buildup and decay curves were measured at $\delta\nu_{excite} = -130$ MHz, which is the frequency of maximum positive DNP enhancement. The buildup curves and their single exponential fit are plotted in Fig. 11a and b for samples measured at 6 K and 20 K respectively. From the comparison between the DNP buildup times of the ^1H (black) and ^2H nuclei (red) at 6 K and 20 K it is evident that the polarization buildup of the ^2H nuclei is much slower than that of the ^1H nuclei. This is perhaps somewhat unexpected as we already saw in Figs. 1a and 2a, that both nuclei reach similar enhancements and have identical DNP spectra. However, the reason for this difference can be understood when realizing that the observed enhancements originate from the bulk nuclei.

| | T_{1e} (msec) | ^1H timescales | | | ^2H timescales | | | | |
		$T_{1,^1H}$ (sec)	T_{bu^1H} (sec)	T_{dec^1H} (sec)	$T_{1,^2H}$ (sec)	T_{bu^2H} (sec)	$T_{dec,^2H}$ (sec)		
6 K	50	28	10	15	135	105	[for $t_{excite} = 3$ s] 70	[for $t_{excite} = 10$ s] 91	[for $t_{excite} = 600$ s] 102
20 K	5	8	5	4	108	103	[for $t_{excite} = 3$ s] 28	-	[for $t_{excite} = 600$ s] 70

Table 3: Summary of the different relaxation times measured for the "H_2O" sample at 6 K and 20 K.

The eSD assisted iCE model implies that the polarized core and local nuclei receive their polarization from their neighboring electrons when those fulfill the respective CE conditions. The bulk nuclei determine the magnitude of the enhanced NMR spectra. This further implies that only a fraction of the electrons are involved in the polarization

enhancement and that each CE electron pair must effectively polarize a large amount of bulk nuclei via the spin diffusion process inside their own nuclear spin bath. As discussed earlier [60], when electrons polarize large amounts of nuclei, and the spin diffusion cross-relaxation rate is fast (which is the case for the 40mM TEMPOL samples), their overall DNP buildup time can be shorter than but of the same order of magnitude of the value of the nuclear bulk T_{1n} of the respective nuclei. It should therefore not surprise us that the ^{1}H and ^{2}H buildup times differ significantly and that they are somewhat shorter than their respective T_{1n}'s . This result would suggest that the two nuclear spin systems are polarized independently each by their own CE electron pairs. However, this cannot be the case when at 6 K the ^{1}H and ^{2}H enhancements are about equal and the DNP spectra are identical, i.e. the ratios between the steady state values of the ^{1}H and ^{2}H polarizations for different MW frequencies $\delta\nu_{excite}$ are all about equal to $\gamma^{^1H}/\gamma^{^2H}$. These observations suggest that there exists a polarization transfer between local ^{1}H nuclei and ^{2}H nuclei in the vicinity of electron pairs.

Another indirect hint of the polarization transfer between ^{1}H and ^{2}H nuclei comes from observing the decay rates of the two nuclei. These decay curves after reaching their steady state DNP enhancements are plotted in Figs. 11c and d for samples measured at 6 K and 20 K respectively. The ^{2}H decay curves measured after $t_{excite} = 3$ sec are added to these figures as inserts. The decay times of the ^{2}H nuclei are much longer than the decay times of the ^{1}H nuclei. The ^{1}H decay times does not depend on the length of t_{excite}, but the ^{2}H decay does. Note that the ^{2}H decay curve in the inset shows a fast, 1-3 sec, increase in the signal at 6 K before it starts to decay with the timescale listed in Table 3. This slight increase before the decay can also be seen in the ^{2}H decay curve measured after $t_{excite} = 10$ sec (Fig. 11c, in teal). Such dependence of the ^{2}H decay rates on the t_{excite} times suggests that the decay rates depend on the state of the polarization of the ^{1}H nuclei in the sample.
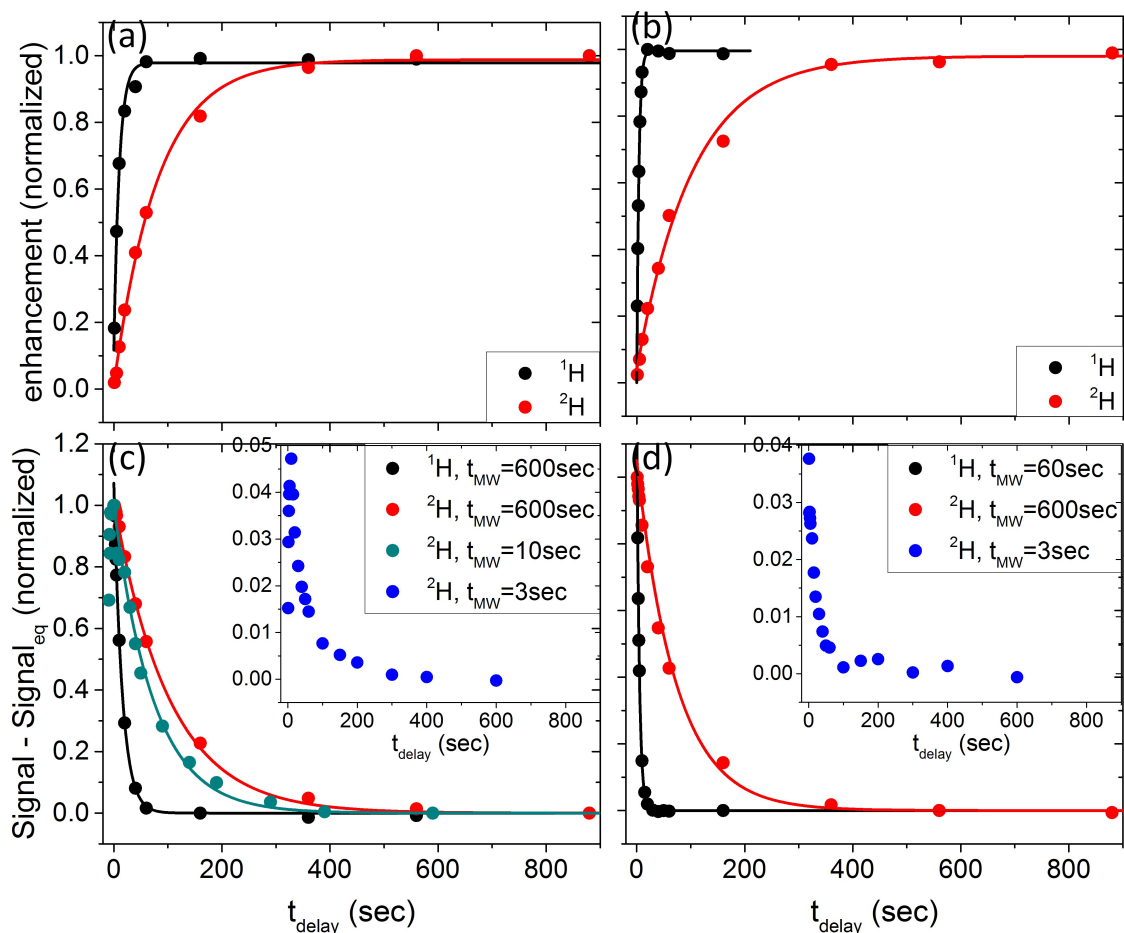
Figure 11: Normalized experimental buildup curves (a, b) and decay curves measured after $t_{excite} = 600$ sec (c, d), measured at the position of maximum positive enhancement, $\delta\nu_{excite} = -130$ MHz. The symbols are experimental data measured for the ^{1}H (black) and ^{2}H (red) nuclei at 6 K (a, c) and 20 K (b, d). The solid lines mono-exponential fits. In panel (c) plotted in teal is the ^{2}H decay after $t_{excite} = 10$ sec, normalized at the maximum. In the insets are plotted decay curves measured after $t_{excite} = 3$ sec. The y-axis of the insets is relative to the steady state enhancement, normalized to 1. The buildup and decay rates are summarized in Table 3.

3.2.2 Polarization exchange between the ^{2}H and ^{1}H nuclei

To further investigate the dependence of the ^{1}H and ^{2}H polarizations in our "H$_2$O" sample at 6 K we performed a set of time dependent experiments that can help us characterize the unique interconnection / "cross-talk" between the polarizations of the two types of nuclei in the sample. A set of experiments was designed for investigating possible ^{1}H-^{2}H polarization exchange processes, in particular in the absence of MW irradiation.

(I) DNP Recovery experiments At first we conducted the classical enhancement-recovery (DNP recovery) experiment introduced by Cox et al. [67]. The pulse sequence of this experiment is shown in Fig. 12d. The experiment starts with DNP enhancement of both the ^{1}H and ^{2}H nuclei via MW irradiation and is followed by a saturation of one of the NMR signals. Subsequently, the recovery of the saturated nuclear signal is monitored by incrementing the t_{d2} delay between the saturation pulses and the nuclear echo detection. Results of such an experiment, where the ^{2}H polarization is monitored following 30 s of MW irradiation (DNP) and subsequent ^{2}H saturation during 7.5 ms, is shown in Fig. 12a. We see that the ^{2}H magnetization partially recovers with a characteristic timescale of 8.5 s, reaching its maximum at $t_{d2} = 30$s. Interestingly, the recovery time of 8.5 sec is about equal to the $T_{1,^1\text{H}}$ of the protons. After the ^{2}H recovery the signal decays with a time constant of 130 s, which is longer than the usual decay time $T_{dec,^2H}$ and close to $T_{1,^2\text{H}}$. The maximum ^{2}H enhancement reached after 30 sec is ~6 which is only 7% of the maximum ^{2}H enhancement detected during the standard DNP experiment. Immediately after the ^{2}H saturation a very small fraction of the ^{1}H polarization disappears and the remaining polarization decays exponentially to thermal equilibrium with the time constant $T_{dec,^1H}$ (data not shown). To further prove that the source of the ^{2}H recovered polarization lies in the ^{1}H pool we acquired the ^{2}H echo signal following a DNP period and a subsequent saturation of both ^{1}H and ^{2}H NMR signals. In this case the ^{2}H polarization hardly recovers, again confirming that the ^{1}H nuclei are the source of the recovered ^{2}H polarization in the above experiment. This experiment is shown in the SI.

Since these type of effects are not seen in solid state NMR experiments of ^{1}H and ^{2}H nuclei without the presence of stable radicals, we believe that the process must be relayed through the unpaired electrons in the sample. Moreover, as the characteristic recovery time of the ^{2}H enhancement is significantly shorter than $T_{1,^2H}$ and $T_{bu,^2H}$ we conclude that the recovery is a result of a ^{1}H-to-^{2}H polarization transfer process that happens in the vicinity of electrons. In that case the average of the local ^{2}H polarizations (which can be positive or negative as will be discussed in Section 4.3.2) is transferred to the bulk deuterons via spin diffusion and their polarization decays to equilibrium in a time close to $T_{1,^2H}$ and $T_{dec,^2H}$ [2, 13, 60, 76, 77] .
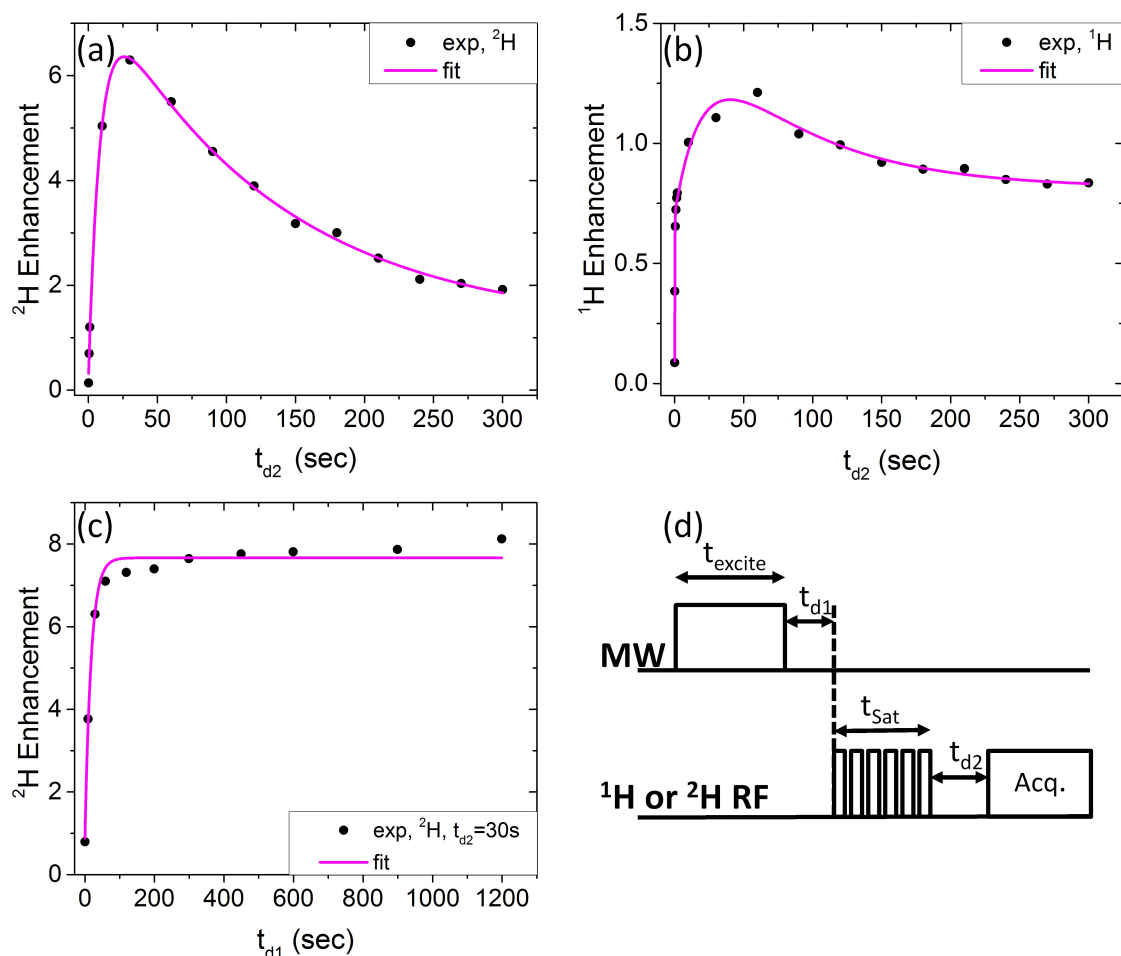
Figure 12: Experimental DNP recovery plots: both nuclei are hyperpolarized, then one is saturated and partially recovers it's polarization before decaying back to its thermal equilibrium value. The pulse sequence appears in panel (d). (a) ^{2}H saturation and detection, (b) ^{1}H saturation and detection, (c) the intensity of the ^{2}H signal measured after $t_{d2} = 30$ sec as a function of the delay time t_{d1}. The black symbols are the experimental data and the magenta lines are the mono/multi-exponential fits. The frequency of MW irradiation was $\delta\nu_{excite} = -130$ MHz. The recovery and decay rates are summarized in Table 4.

Next we conducted the reverse experiment where we saturated the ^{1}H nuclei after a DNP MW irradiation period and followed their recovery, as shown on Fig. 12b. In this case we used $t_{excite} = 600$s to ensure maximum possible ^{2}H polarization. While qualitatively we observed a similar effect as for the ^{2}H recovery in figure 6(a) there are two significant differences: (i) The overall recovered ^{1}H enhancement that is obtained is much smaller (~1.2) than in the ^{2}H case and (ii) its time dependence does not follow a simple bi-exponential behavior, with one rising and one decaying exponential, as was observed in the ^{2}H case. The small ^{1}H recovery after saturation is perhaps not surprising when we realize that after the DNP process the actual value of the enhanced ^{2}H polarization is

only about ten times larger than the equilibrium ^{1}H polarization, because of the large $\gamma_{^1H}/\gamma_{^2H}$ ratio.

The time behavior of the ^{1}H enhancement clearly shows three time processes: A fast rise with a time constant smaller than 0.5 s, a second increase with a time constant a bit longer than the 8.5 s, the time constant of the polarization transfer process measured above, and a decay to equilibrium with a time 78 s, which is longer than $T_{1,^1H} \approx 30$ s. The first fast component can be attributed to the dipolar driven polarization transfer from the non-saturated (far off-resonance due to strong hyperfine interaction) core nuclei to the local nuclei. To verify this a similar effect of a fast reappearance of ^{1}H polarization after saturation was also observed in the "fully protonated" sample without deuterons. In this experiment the fast reappearance of some ^{1}H polarization happened with a time constant of 0.08 sec (see SI). The slower rising component can then be assigned to the ^{2}H-to-^{1}H polarization transfer process. Although the enhancement of the ^{1}H signal is small it decays in a time longer than $T_{1,^1H}$, suggesting that the bulk ^{2}H polarization, with a decay time much longer than $T_{1,^1H}$, maintains the local ^{1}H nuclei above thermal equilibrium for longer. This overall ^{1}H response indicates that the very small ^{2}H-to-^{1}H polarization transfer, with a rise time shorter than $T_{bu,^1H}$ and a decay time longer than $T_{dec,^1H}$, does not take place in the bulk proton bath but rather close to the CE electron pairs.

In a related experiment, with results shown in Fig. 12c, the amount of recovered ^{2}H magnetization, after saturation, was monitored as function of t_{excite}, while the delay between the saturation and the detection pulses was set to $t_{d2} = 30$ sec, which corresponds to the time of maximum recovery of ^{2}H polarization in Fig. 12a. The maximum observed enhancement reaches a steady state value of ~8 for $t_{excite} \approx 100$ sec. The rise time of this ^{2}H polarization recovery process could be fitted to a single exponential with a time constant of 18 sec. The similarity between this time constant and the buildup time of the protons tells us that the amount of recovered ^{2}H magnetization is about proportional to the magnitude of the ^{1}H polarization just after ^{2}H saturation. Because we cannot detect the polarization of the local versus bulk nuclei separately, we should not attempt to make quantitative statements about the actual amounts of transferred polarization. For the same reason it is not possible at this stage to say something quantitative about the spin diffusion driven transfer of local to bulk polarization. However, these experiments do show that even without MW irradiation or depolarized electrons, polarization can be transferred between the protons and the deuterons as long as one of the nuclei is not at thermal equilibrium. At equilibrium the polarization exchange stops and the ratio between the ^{1}H and ^{2}H polarizations is again equal to $\gamma_{^1H}/\gamma_{^2H}$.

(II) Constant saturation experiments　 Our next experiments were once again aimed to show the intricate interconnection / "cross-talk" between ^{1}H and ^{2}H nuclear pools in

our sample by recording the decay of the hyperpolarized NMR signals under varying conditions. From the data shown up to this point we understand that there exists a ^{1}H-to-^{2}H polarization exchange process in the vicinity of electrons and that this process can be examined by measuring the local and bulk nuclear polarizations. A possible way of following one aspect of this exchange process is to measure the rate of depolarization of one type of enhanced nuclei as a function of the state of enhancement of the other type of nuclei. Here we did so by comparing the regular rate of decay of the ^{2}H polarization after a standard DNP experiments with the decay in the presence of a repetitive ^{1}H saturation train of pulses of length t_{sat}. This pulse train ensured that the ^{1}H polarization is kept at zero during the decay of the ^{2}H hyperpolarization. We then conducted the opposite experiment, saturating ^{2}H and measuring the ^{1}H signal. These experiments are presented in Fig. 13, where (in a) we show the decay of the ^{2}H signal, while saturating ^{1}H, and (in b) also the ^{1}H signal decay, while saturating ^{2}H. In both cases the decay could be satisfactory fitted by a single exponential. The difference between the decay timescales with and without the saturation was striking: while the regular decay constant of the hyperpolarized ^{2}H signal (Table 4) was 102 sec, in the presence of the ^{1}H saturation train it was reduced to 8.5 sec.

Similarly when we observed the ^{1}H signal in the presence of the repeating ^{2}H saturation train we detected a very fast decay of the ^{1}H polarization to zero with a time constant of 4.3 sec. This should be compared to the 15 sec decay time for the ^{1}H nuclei from the steady state (for $t_{excite} = 600$ sec) enhancement in the unperturbed system.

Another important outcome of these experiments is the unexpected result that, while in the absence of ^{1}H saturation the ^{2}H magnetization decays, as expected, to its thermal equilibrium value in the presence of ^{1}H pulses the ^{2}H magnetization decays to zero; i.e. it is possible to saturate the ^{2}H NMR signal by RF irradiation at the ^{1}H frequency.
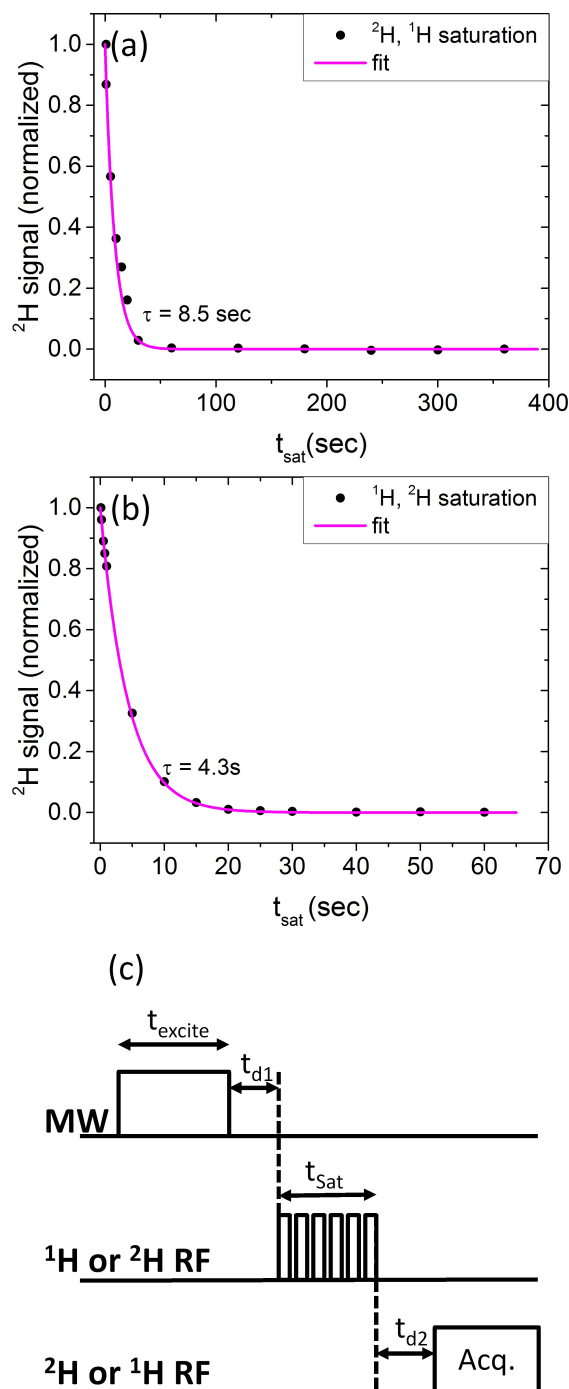
Figure 13: (a) Decay of ^{2}H polarization in the presence of a continuous ^{1}H saturation train. (b) Decay of ^{1}H polarization in the presence of a continuous ^{2}H saturation train. (c) Pulse sequence of the experiments presented in (a) and (b). Both nuclei are hyperpolarized to their respective steady state value prior to the experiment. The detected nucleus is saturated indirectly and reaches a steady state value of zero within τ listed in the figure. The black symbols are the experimental data and the magenta lines are the mono-exponential fits. The decay rates are summarized in Table 3.

Experiment	Time-constant (sec)
DNP recovery (^{2}H recovery)	8.5
DNP recovery (^{2}H decay)	130
DNP recovery (^{1}H recovery, fast component)	0.13
DNP recovery (^{1}H, recovery, slow component)	20
DNP recovery (^{1}H, decay)	78
Constant saturation of ^{1}H (^{2}H decay)	8.5
Constant saturation of ^{2}H (^{1}H decay)	4.3

Table 4: Summary of the timescales observed in different ^{1}H-^{2}H polarization "cross-talk" experiments performed at 6 K on the "H$_2$O" sample.

3.3 Summary of experimental results

At this point we can summarize our observations concerning the differences between the ELDOR and DNP spectra of the "H$_2$O" sample obtained at 6 K and 20 K and their time dependent DNP enhancements measured at 6 K:

(i). The steady state ELDOR spectra could be analyzed relying on our electron depolarization model, involving an eSD coefficient Λ^{eDS}, a T$_{2e}$ value and an effective electron-proton hyperfine interaction as fitting parameters. Taking the measured change in the T$_{1e}$ value with temperature into account, we succeeded to reproduce the ELDOR spectra and from them the electron depolarization profiles for different $\delta\nu_{excite}$ values. This result suggests that the electronic polarization distributions are determined by the MW irradiation, the eSD process and the protons in the system.

(ii). The calculated depolarization profiles, together with their fitting parameters Λ^{eSD} and T$_{2e}$, enabled us to predict the shapes of the ^{1}H-DNP and ^{2}H-DNP spectra, considering only the iCE process. These shapes were compared with the normalized experimental DNP spectra obtained at steady state and revealed that the two (at 6 K and 20 K) calculated depolarization profiles reconstruct the main spectral features of the ^{1}H-DNP spectra at 6 K and 20 K. Similarly, the ^{2}H-DNP spectrum at 20 K showed the same features as its calculated ^{2}H-DNP counter part. However, at 6 K the steady state ^{2}H-DNP spectrum resembled the ^{1}H-DNP spectrum at that temperature, an effect that could not be reproduced in our calculations.

(iii) The enhancements of the steady state DNP spectra were all of the same order of magnitude, in particular those of the ^{1}H- and ^{2}H-spectra at 6 K.

(iv) The ^{2}H-DNP spectra measured on the "fully deuterated" sample look very similar to the ^{2}H-DNP spectra of the "H$_2$O" and "D$_2$O" samples at 20 K, and of the "H$_2$O" sample at 6 K measured after a short MW irradiation periods. All these spectra could successfully be simulated using our iCE - ELDOR model. The "D$_2$O" sample behaves very similarly to the "H$_2$O" sample, although a smaller hyperfine interaction between the ^{1}H nuclei and the radicals than used for the "H$_2$O" ELDOR spectra was required to fit

the DNP spectra of the "D$_2$O" sample.

(v) The buildup times of all DNP spectra were slightly shorter than their corresponding nuclear T$_{1n}$'s but of the same order of magnitude. Here we must emphasize that even at 6 K, where the steady state ^{1}H- and ^{2}H-DNP spectra are identical, the proton and deuterium buildup times are very different, 10 sec and 105 sec, respectively.

(vi) Although as described in (ii) the steady state ^{2}H-DNP spectrum at 6 K resembles the ^{1}H-DNP spectrum, after a short MW irradiation period of 1s this ^{2}H-DNP spectrum resembles the spectrum expected from the ^{2}H-iCE process. Furthermore the characteristic decay time of the deuterium enhancement varies for different MW irradiation lengths. For a MW irradiation period of 3 s the decay time is 70 s, significantly shorter than the $T_{1,^2H}$ =135 s , and for a MW period of 600 s the decay time is 102 s. An intermediate value of the decay time is measured after 10 sec of MW irradiation.

(vii) From our time domain experiments it follows that after a polarization enhancement followed by a saturation of one type of nucleus the polarization of the other nucleus shows a small but significant recovery. The recovery time for ^{2}H is shorter than its T$_{1,^2H}$ and for ^{1}H of the order of its T$_{1,^1H}$.

(viii) Finally, continuous saturation of the ^{1}H nuclei results in a total depolarization ($P_{^2H} = 0$) of ^{2}H in a very short time scale of ~8.5 sec. In the reverse experiment the continuous saturation of the ^{2}H nuclei results in a decay to zero of the ^{1}H polarization again with a very short decay constant of ~4.3s.

4 Theoretical discussion

4.1 Conclusions following the experimental results

In this section we will describe a theoretical framework which we think can explain the majority of our results. The discussion will be mainly qualitative, as we currently do not have the necessary model for a complete quantitative analysis.

From the summary of the experimental results from the "H$_2$O" sample we can arrive at the following conclusions:

1. From (ii) it follows that at 20 K the polarizations of the ^{1}H and ^{2}H spins in the sample are both determined by the electron depolarization, but behave independent of each other. Although the depolarization profiles are partially influenced by the presence of the^{1}H spins in the sample, they determine the ^{1}H- and ^{2}H-DNP spectra via the two independent iCE processes respectively.

2. Also from (ii) we learn that at 6 K this is not the case. While the electrons and ^{1}H spins are correlated via their own ^{1}H-iCE mechanism as at 20 K, the ^{2}H spins are strongly influenced by the presence of the ^{1}H spins at 6 K. From (ii) it even follows that the enhancements as a function of the MW frequency are almost identical. Thus by

cooling the sample from 20 K to 6 K the ^{2}H-iCE mechanism seems to be suppressed by a mechanism that connects ^{1}H and ^{2}H polarizations. This suggests that there are two ^{2}H enhancement mechanisms, the ^{2}H-iCE mechanism and a DNP-exchange mechanism that can compete in the enhancement of ^{2}H nuclei. This notion is strengthened by the fact reported in (iv) that at short MW irradiation times the ^{2}H-iCE process dominates the ^{2}H enhancement, while at long times this DNP-exchange mechanism seems to be dominant.

3. The fact summarized in (v) that the buildup times of the ^{1}H and ^{2}H polarizations at 6 K are very different suggests that their enhancement equilibration originates from localized polarization sources. This assures that the homonuclear spin diffusion processes are still responsible for the difference in the buildup times of the bulk polarization and that the equilibration is not a simple direct heteronuclear spin diffusion process. This indicates that the DNP-exchange process is governed by isolated groups of electrons in the sample still allowing the two spin diffusion processes to determine the buildup times.

4. These groups of electrons succeed to equalize, according to (iii), the **bulk** enhancement of the ^{2}H spins to the ^{1}H spins. In addition, following (vi and vii), they succeed to transfer the polarization of one type of nucleus to the other type after saturation of the latter and to fully saturate the bulk polarization of one type of nucleus during active saturation of the other nucleus.

As was mentioned in the introduction, similar results have been reported previously with different radicals and nuclei. These results were typically explained by the TM model where the temperature of the different nuclear spins equilibrates with the electron non-Zeeman temperature. The models also predict different buildup and decay rates for two different types of nuclei [78]. In a recent work, however, we have shown that the electron depolarization profiles we obtain are inconsistent with the existence of an electron non-Zeeman temperature [23]. We therefore are looking for a different theoretical framework for explaining our results. Our approach will be based on the existence of the hnCE [61]. We will search for groups of electrons that can cause the ^{2}H spins to become polarized to a degree that is, at least, proportional to the ^{1}H polarization and that together with the spin diffusion process are responsible for the DNP-exchange mechanism.

In the following section we will first discuss the CE with I=1 nuclei and then show that the electron pairs satisfying the heteronuclear (hn) CE condition are capable of providing their neighboring ^{2}H spins with a polarization proportional to the polarization of their neighboring ^{1}H spins. In this section the basics of the hnCE process in small model $\{e - e - (^1\text{H}_3, {}^2\text{H})\}$ systems will be presented and will be followed by a qualitative discussion about the possible consequences of this process for the bulk polarizations in real samples.

4.2 The cross effect for nuclei with I=1

In Ref. [19] we introduced the iCE mechanism for I=1/2 nuclei in amorphous solids by assuming that the nuclear bulk polarization is proportional to the average of the polarizations of the nuclei coupled to electron spin pairs at the CE condition with different polarizations. Considering an electron-electron-nucleus three-spin system ($\{e_a - e_b - n\}$ with resonance frequencies satisfying $\delta\nu_a - \delta\nu_b = \nu_n$ ($\delta\nu_b > \delta\nu_a$) and with fixed polarizations P_i with $i = a, b$, we showed that at steady state the nuclear polarization, at the high temperature approximation, becomes

$$P_n = \frac{P_b - P_a}{1 - P_a P_b}.\tag{5}$$

In the same study we also showed this to be true for the dCE.

Following the same arguments as in Ref. [19] we can conduct a similar calculation for a nucleus with I=1 with eigenstates $|+1>$, $|0>$ and $|-1>$. In this case, with $\chi_{a,b} = \alpha, \beta$ and $\chi_n == 1, 0, -1$, we get at steady state that

$$\frac{p(\alpha_a, \chi_b, \chi_n)}{p(\beta_a, \chi_b, \chi_n)} = \eta_a \;\; ; \;\; \frac{p(\chi_a, \alpha_b, \chi_n)}{p(\chi_a, \beta_b, \chi_n)} = \eta_b \;\; ; \;\; \frac{p(\chi_a, \chi_b, 0_n)}{p(\chi_a, \chi_b, +1_n)} = \eta_n \;\; ; \;\; \frac{p(\chi_a, \chi_b, -1_n)}{p(\chi_a, \chi_b, 0_n)}) = \eta_n^2\tag{6}$$

The resulting populations are then equal to

$$p(\beta, \beta, +1) = c \; ; \; p(\alpha, \beta, +1) = c\eta_a \; ; \; p(\beta, \alpha, +1) = c\eta_b \; ; \; p(\alpha, \alpha, +1) = c\eta_a\eta_b$$
$$p(\beta, \beta, 0) = c\eta_n \; ; \; p(\alpha, \beta, 0) = c\eta_a\eta_n \; ; \; p(\beta, \alpha, 0) = c\eta_b\eta_n \; ; \; p(\alpha, \alpha, 0) = c\eta_a\eta_b\eta_n$$
$$p(\beta, \beta, -1) = c\eta_n^2 \; ; \; p(\alpha, \beta, -1) = c\eta_a\eta_n^2 \; ; \; p(\beta, \alpha, -1) = c\eta_b\eta_n^2 \; ; \; p(\alpha, \alpha, -1) = c\eta_a\eta_b\eta_n^2,\tag{7}$$

resulting in the polarizations

$$P_a = (1 - \eta_a)/(1 + \eta_a)$$
$$P_b = (1 - \eta_b)/(1 + \eta_b)$$
$$P_n = (1 - \eta_n^2)/(1 + \eta_n + \eta_n^2)\tag{8}$$

with the normalization factor c equal $[(1 + \eta_a + \eta_b + \eta_a\eta_b)(1 + \eta_n + \eta_n^2)]^{-1}$. The ideal CE condition is here defined by an energy matching of the state $|\alpha, \beta, +1 >$ with $|\beta, \alpha, 0 >$ and at the same time $|\alpha, \beta, 0 >$ with $|\beta, \alpha, -1 >$ ignoring any significant nuclear quadrupolar shifts. The consequence of these matching conditions is that

$$p(\alpha, \beta, +1) = p(\beta, \alpha, 0) \;\; ; \;\; p(\alpha, \beta, 0) = p(\beta, \alpha, -1)\tag{9}$$

and thus

$$c\eta_a = c\eta_b\eta_n \;\; ; \;\; c\eta_a\eta_n = c\eta_b\eta_n^2. \tag{10}$$

Using this relationship between η_n and η_a and η_b, we calculate the two sides of equation 5 using the expressions for the polarizations given in eq. 8. We obtain a dependence between them that does not result in a simple expression, however it can be simplified for high temperatures by taking η_a and η_b values close to 1. Replacing these factors with $\eta_a = (1 - x_a)$ and $\eta_b = (1 - x_b)$ and taking $x_a, x_b \ll 1$, a straightforward calculation results in

$$\frac{P_b - P_a}{1 - P_a P_b} \cong \frac{x_b - x_a}{2} \;\; ; \;\; P_n \cong \frac{2(x_b - x_a)}{3} \tag{11}$$

and thus

$$P_n \cong \frac{4}{3}\frac{P_b - P_a}{1 - P_a P_b}. \tag{12}$$

The validity of this relationship can be investigated by performing simulations of $P_{^2H}$, the polarization of a ^{2}H nucleus, as a function of fixed values for $P_{a/b}$. To do so we calculated the $P_{^2H}$ and $P_{a/b}$ values of a three-spin system $\{e_a - e_b - {}^2\text{H}\}$, at the ^{2}H-CE condition as a function of the MW irradiation frequency, $\delta\nu_{excite}$, leaving out values of $\delta\nu_{excite}$ that correspond to SE enhancement. In Fig. 14 we plotted $P_{^2H}$ as a function of $\frac{P_b - P_a}{1 - P_a P_b}$, and we observe that the slope is indeed $\frac{4}{3}$. The dashed gray line corresponds to $P_{^2H} = \frac{4}{3}\frac{P_b - P_a}{1 - P_a P_b}$, confirming eq. 12. This equation was checked for a wide variety of interaction and relaxation parameters, and we found it to be true in all cases. Note that the calculations were conducted on the dCE-DNP, but are also correct for the iCE-DNP mechanism, as was shown in Ref. [19]. Note also that the line starts to deviate from a straight line and show some curvature when the CE condition is not entirely fulfilled or under 6 K where we start to deviate from the high temperature approximation (not shown).
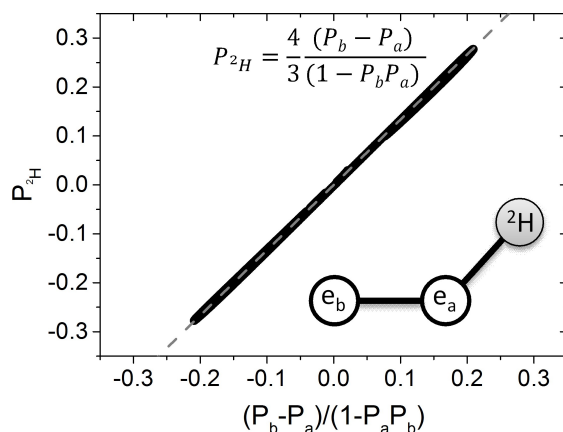
Figure 14: The calculated nuclear polarization $P_{^2H}$ as a function of $\frac{P_b - P_a}{1 - P_a P_b}$ for a three spin system of $\{e_a - e_b - {}^2H\}$, where ${}^2H$ is spin $I = 1$ (black symbols). A sketch of the spin system is plotted: Two electrons, dipolar-coupled, hyperfine-coupled to one ${}^2H$ nucleus. The solid lines represent dipolar or hyperfine interactions. In the dashed gray line we plotted $\frac{4}{3} \frac{P_b - P_a}{1 - P_a P_b}$, confirming the slope of $\frac{4}{3}$ that arises because of the spin $I = 1$ nucleus. The parameters of the calculation are: $\delta\nu_a = 0$ MHz, $\delta\nu_b = 22$ MHz, $\nu_{^2H} = 22$ MHz, $D_{ab} = 3$ MHz, $A_{z,aD} = A_{z,bD} = 0$ MHz, $A_{aD}^{\pm} = 0.5$ MHz, $A_{bD}^{\pm} = 0$ MHz, $T_{1e} = 10$ msec, $T_{1,^2H} = 100$ sec, $T_{2e} = 20$ usec, $T_{2n} = 100$ usec, $T = 10$ K, $\delta\nu_1 = 0.5$ MHz, $t_{excite} = 10^5$ sec, $\delta\nu_{excite}$ was between -60 MHz and 60 MHz, excluding ${}^2H$-SE transitions.

4.3 The heteronuclear cross effect

4.3.1 Steady state conditions

In Ref. [61] we introduced the hnCE for ${}^1H$ and ${}^{13}C$ nuclei. There we showed that in a four spin system of the form $\{e_a - e_b - ({}^1H, {}^{13}C)\}$ there are high order CE processes simultaneously involving both nuclei when $\delta\nu_b - \delta\nu_a = \delta\nu_{^1H} \pm \delta\nu_{^{13}C}$ ($\delta\nu_b > \delta\nu_a$). In this work we expand this hnCE mechanism by describing it for ${}^1H$ (I=1/2) and ${}^2H$ (I=1) nuclei. In the $\{e_a - e_b - ({}^1H, {}^2H)\}$ spin system the two hnCE conditions are defined as:

$$\delta\nu_b - \delta\nu_a = \delta\nu_{^1H} \pm \delta\nu_{^2H} \tag{13}$$

where ($\delta\nu_b > \delta\nu_a$). We will denote these two conditions as hnCE$^+$ and hnCE$^-$ according to the choice for $\pm$. It should be noted that the probability of occurrence of these conditions is $f(\delta\nu_e)f(\delta\nu_e \pm \delta\nu_{^1H} \pm \delta\nu_{^2H})$, where $f(\delta\nu_e)$ is the probability of finding an electron at a frequency $\delta\nu_e$, and the frequency matching of the hnCE$^{\pm}$ conditions is rather narrow, because the mixing of the states is proportional to $atan(\frac{A_{eH}^{\pm}}{\delta\nu_{^1H}} \frac{A_{eD}^{\pm}}{\delta\nu_{^2H}} \frac{\Delta_{ab}}{|\delta\nu_a - \delta\nu_b| - |\delta\nu_{^1H} \pm \delta\nu_D|})$ which is quite small. Defining the eigenstates of this system and their populations in terms of the product wavefunctions of the $|\alpha_{^1H}>$ and $|\beta_{^1H}>$ states of ${}^1H$ and $|1_{^2H}>$, $|0_{^2H}>$ and

$|-1_{2H}>$ of ^{2}H, we find that at each CE condition there are two sets of degenerate energy levels. At these conditions the populations p of the degenerate levels become equal.

For hnCE$^+$

$$p(\alpha_a, \beta_b, \alpha_{1H}, 0_{2H}) = p(\beta_a, \alpha_b, \beta_{1H}, +1_{2H}) \; ; \; p(\alpha_a, \beta_b, \alpha_{1H}, -1_{2H}) = p(\beta_a, \alpha_b, \beta_{1H}, 0_{2H}) \tag{14}$$

and for hnCE$^-$

$$p(\alpha_a, \beta_b, \alpha_{1H}, +1_{2H}) = p(\beta_a, \alpha_b, \beta_{1H}, 0_{2H}) \; ; \; p(\alpha_a, \beta_b, \alpha_{1H}, 0_{2H}) = p(\beta_a, \alpha_b, \beta_{1H}, -1_{2H}). \tag{15}$$

It would be interesting to derive from these conditions analytic expressions that correlate the four polarizations of the system under steady state conditions in the way we did for the ^{2}H-CE processes in section 4.2. However, here we will restrict ourselves to discussing the hnCE process only in accordance with numerical simulations. To do so we consider two types of spin situations: (I) systems where P_a and P_b are fixed and we calculate the resulting values of P_{1H} and P_{2H} and (II) where in addition to the fixed P_a and P_b values we also fix P_{1H} and calculate the resulting P_{2H}.

For spin system (I) we use the six spin system, $\{e_a - e_b - (^1H_3, {}^2H)\}$, and we fix the polarizations of e_a and e_b by irradiating directly on or near one of the electrons, or by off-resonance irradiation on both. The three ^{1}H nuclei are hyperfine coupled to e_b and all reach the same polarization value, referred to as P_{1H}, because they are connected by dipolar cross-relaxation with a short T_{1d}^{1H} value. The resulting P_{1H} and P_{2H} are shown in Fig. 15 as a function of $\frac{P_b - P_a}{1 - P_a P_b}$ for the hnCE$^-$ (a, c) and hnCE$^+$(b, d) conditions. Notice how at the hnCE$^-$condition the sign of P_{2H} is opposite to the sign of P_{1H} and at the hnCE$^+$condition their signs are the same and that the absolute values of the nuclear polarizations increase (decrease) simultaneously for increasing (decreasing) $P_a - P_b$ values. These phenomena were also shown in our previous publication about the hnCE for two spin I=1/2 nuclei [61]. We also previously showed that the steady state nuclear polarizations depend strongly on the spin-lattice relaxation times of the nuclei, such that most of the polarization is transferred to the nucleus with the longer T_{1n}. This is valid also in this case, and can be seen in Fig 15. In the top row we plot the P_{1H} and P_{2H} values for $T_{1,^1H} = T_{1,^2H}$, and in the bottom row we plot the same for $T_{1,^1H} < T_{1,^2H}$. Comparing the two rows, we see that by lowering $T_{1,^1H}$ such that $T_{1,^1H} < T_{1,^2H}$, P_{1H} decreases while P_{2H} increases.
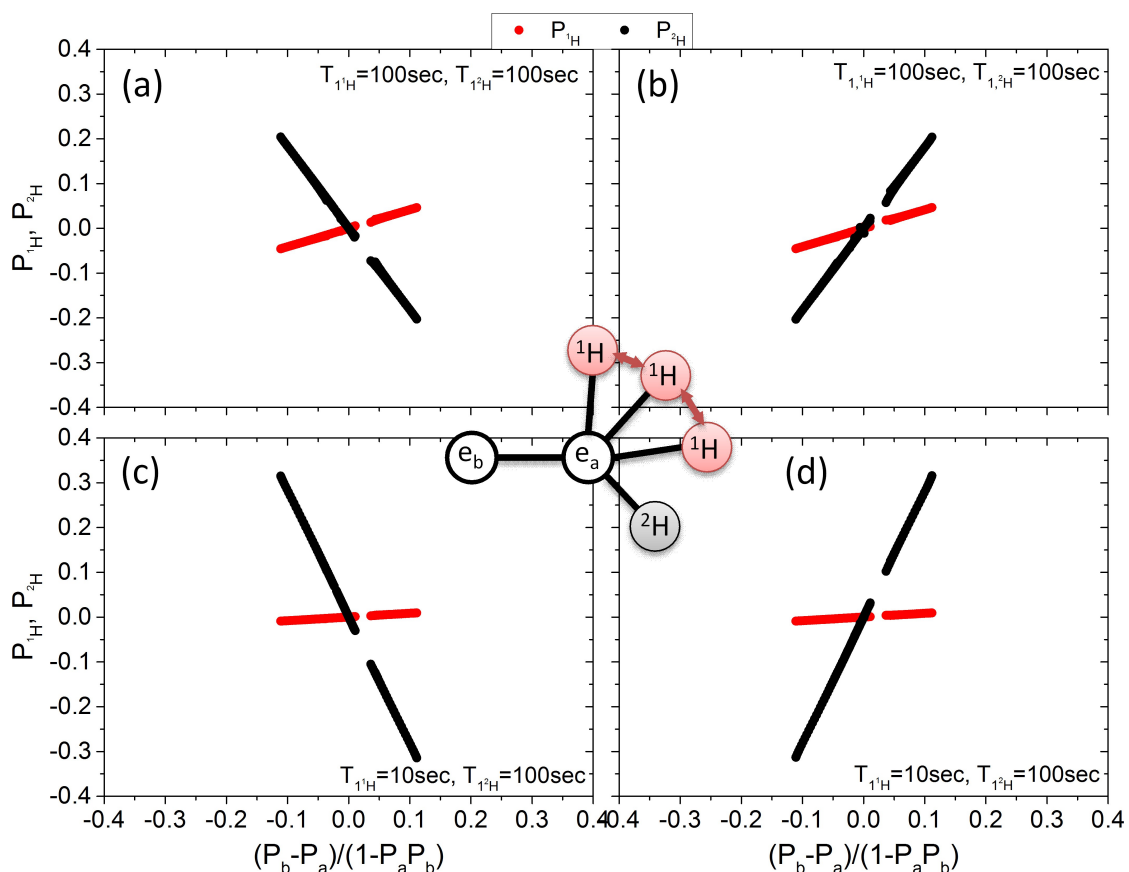
Figure 15: The calculated nuclear polarizations $P_{^1H}$ (black symbols) and $P_{^2H}$ (red symbols) as a function of $\frac{P_b - P_a}{1 - P_a P_b}$ for the six-spin system of $\{e_a - e_b - (^1H_3, {}^2H)\}$, where ^2H is spin $I = 1$, for the hnCE$^-$ (a, c) and hnCE$^+$(b, d) conditions. A sketch of the spin system is plotted: Two electrons, dipolar-coupled, hyperfine-coupled to three ^1H nuclei and one ^2H nucleus. The solid lines represent dipolar or hyperfine interactions. The red two-sided arrows represent cross-relaxation between the ^1H nuclei. In (a, b) $T_{1,^1H} = T_{1,^2H} = 100$ sec, and in (c, d) $T_{1,^1H} = 10$ sec and $T_{1,^2H} = 100$ sec. The parameters of the calculation are: $\delta\nu_a = 0$ MHz, $\delta\nu_b = 121.9629719$ MHz for hnCE$^-$ and $\delta\nu_b = 165.9734609$ MHz for hnCE$^+$, $\nu_{^1H} = 144$ MHz, $\nu_{^2H} = 22$ MHz, $\Delta_{ab} = 3$ MHz, $A_{z,aH,i} = A_{z,bH,i} = 0$ MHz for $i = 1-3$, $A^{\pm}_{aH,1} = 0.5$ MHz, $A^{\pm}_{aH,2} = 0.4$ MHz, $A^{\pm}_{aH,3} = 0.45$ MHz, $A^{\pm}_{bH,i} = 0$ MHz for $i = 1-3$, $A_{z,aD} = A_{z,bD} = 0$ MHz, $A^{\pm}_{aD} = 0.5$ MHz, $A^{\pm}_{bD} = 0$ MHz, $T_{1e} = 10$ msec, $T_{1,^1H} = 10$ sec, $T_{1,^2H} = 100$ sec, $T^H_{1d} = 1$ msec, $T_{2e} = 20$ usec, $T_{2n} = 100$ usec, $T = 10$ K, $\delta\nu_1 = 0.5$ MHz, $t_{excite} = 10^5$ sec, $\delta\nu_{excite}$ was between -111 MHz and 258 MHz, excluding ^1H-SE and ^2H-SE transitions.

For spin system (II) we extend the spin system to $\{e_c - e_a - e_b - (^1H_3, {}^2H) - e_d\}$. Here e_c is introduced to fix the populations P_a and P_b via a eSD type of processes. This electron is selectively saturated and is only connected to electrons e_a and e_b via cross-relaxation, T_{1D}. Electron e_d is introduced to constrain $P_{^1H}$ via the ^1H-SE-DNP mechanism. This is done by coupling e_d to the ^1H nuclei via a hyperfine interaction and choosing its

resonance frequency such that $\delta\nu_d - \delta\nu_c = \pm\delta\nu_H$. Irradiation at $\delta\nu_c$ saturates electron e_c and simultaneously creates a SE-DNP process polarizing the ^{1}H nuclei with the help of e_d. As before, the three ^{1}H nuclei all reach the same polarization value, referred to as P_{1H}, via a short T_{1d}^{1H} value. In this way it was possible to partially control the value of P_{1H}.

Results of these simulations are shown in Fig. 16 for a set of relaxation parameters given in the figure caption. Both panels show P_{2H} as a function of $\frac{P_b - P_a}{1 - P_a P_b}$, where each line connects the P_{2H} results for a different value of P_{1H}. The top panel (Fig. 16a) shows the hnCE$^-$ condition, and the bottom panel (Fig. 16b) shows the hnCE$^+$condition. The figure shows that P_{2H} depends both on the difference in electron polarization $P_b - P_a$ and on the value of P_{1H}. The lines for each individual P_{1H} value for the hnCE$^\pm$ conditions are almost straight,

$$P_{2H}(hnCE)^\pm \approx x^\pm(P_{1H}) \cdot P_{1H} + y^\pm \frac{P_a - P_b}{1 - P_a P_b},$$

with $x^+ = -x^-$ and $y^+ = -y^-$. The values of $x^+(P_{1H})$ as function of P_{1H} are close to 4/3 and the signs of $x^\pm(P_{1H})$ and $y^\pm$ are opposite. We found that In our samples where the hnCE$^\pm$ are simultaneously present, and possibly active, it is not trivial to consider these observations and use them for creating a model that defines the action of these conditions together with spectral and spin diffusion process and can explain the steady state enhancement equilibration obtained here at 6 K and reported before by many groups.
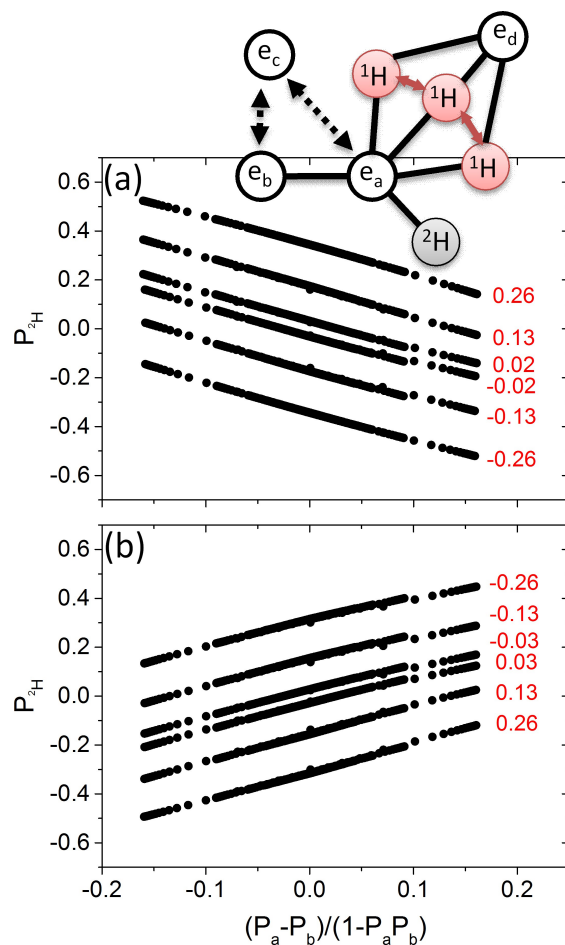
Figure 16: The calculated nuclear polarization P_{2H} as a function of $\frac{P_b - P_a}{1 - P_a P_b}$ for the eight-spin system of $\{e_c - e_a - e_b - ({}^1H_3, {}^2H) - e_d$, where ${}^2H$ is spin $I = 1$, for the hnCE$^-$ (a) and hnCE$^+$(b) conditions. e_c is introduced in order to fix P_a and P_b and is only connected to electrons e_a and e_b via cross-relaxation, T_{1x}. e_d is introduced to fix P_H via the ${}^1H$-SE-DNP mechanism, and is not connected to any of the other electrons or to the ${}^2H$ nucleus. A sketch of the spin system is plotted. The solid lines represent dipolar or hyperfine interactions. The red two-sided arrows represent cross-relaxation between the ${}^1H$ nuclei, the black two-sided dashed arrows represent cross-relaxation between e_c and e_a/e_b . Each diagonal line was calculated for a different value of P_H. The parameters of the calculation are: $\delta\nu_a = 0$ MHz, $\delta\nu_b = 121.9638402$ MHz for hnCE$^-$ and $\delta\nu_b = 165.9734609$ MHz for hnCE$^+$, $\delta\nu_c = 400 \pm 144$ MHz for negative or positive ${}^1H$-SE enhancement with electron e_d, $\delta\nu_d = 400$ MHz, $\nu_{1H} = 144$ MHz, $\nu_{2H} = 22$ MHz, $\Delta_{ab} = 3$ MHz, $A_{z,eH,i} = 0$ MHz for $e = a - d$ and $i = 1 - 3$, $A^{\pm}_{aH,1} = 0.5$ MHz, $A^{\pm}_{aH,2} = A^{\pm}_{aH,3} = 0$ MHz, $A^{\pm}_{dH,1} = 1$ MHz, $A^{\pm}_{dH,2} = 1.1$ MHz, $A^{\pm}_{dH,3} = 0.9$ MHz, $A^{\pm}_{bH,i} = A^{\pm}_{cH,i} = 0$ MHz for $i = 1 - 3$, $A_{z,eD} = 0$ MHz for $e = a - d$, $A^{\pm}_{aD} = 0.25$ MHz, $A^{\pm}_{eD} = 0$ MHz for $e = b - d$, $T_{1e} = 10$ msec, $T_{1,{}^1H} = 10$ sec, $T_{1,{}^2H} = 100$ sec, $T^H_{1d} = 1$ msec, $T_{2e} = 20$ usec, $T_{2n} = 100$ usec, $T = 10$ K, $\delta\nu_1 = 0.5$ MHz, $t_{excite} = 10^5$ sec, $\delta\nu_{excite} = 400 \pm 144$ MHz for negative or positive ${}^1H$-SE enhancement, respectively.

4.3.2 Dynamic conditions

In the conclusion number (4) in Section 4 we summarized the temporal effects demonstrating the cross-talk between the ^{1}H and ^{2}H polarizations. We showed that after DNP enhancement and single nuclear saturation the polarization of the saturated nuclei partially recover on the account of the polarization of the other type nuclei in the sample (Fig. 12). We also showed that constant active saturation on one nuclear type results in a quick saturation of the other (Fig. 13). Most of these effects were believed to take place between nuclei close to electrons and we therefore assume that the hnCE mechanism should be the source of these effects. To show that the temporal phenomena can indeed have their origin close to the hnCE electron pairs, we simulated the nuclear polarizations for the spin system $\{e_a - e_b - (^1\text{H}_3, ^2\text{H})\}$ defined above for the two types of time dependent experiments. In particular we fix the values of P_a and P_b by MW irradiation and follow the $P_{^1\text{H}}(t_{2d})$ and $P_{^2\text{H}}(t_{d2})$ polarizations for two different conditions: one where $P_{^2\text{H}}(0) = 0$, corresponding to a ^{2}H presaturation (DNP recovery) experiment , and the other where $P_{^1\text{H}}(t_{2d})$ is kept equal to zero, corresponding to the continuous ^{1}H saturation experiment. The results are shown in Figs. 17 and Fig. 18, respectively, where (a) represents the results for the hnCE$^-$condition and (b) for the hnCE$^+$condition.

We see in these two figures that the time evolutions of $P_{^2\text{H}}(t_{d2})$ resemble the experimental observations, namely the partial ^{2}H polarization recovery in the first figure and the fast total ^{2}H depolarization in the second.

In Fig. 17 we see that the recovered ^{2}H polarization can have the same or opposite sign of the ^{1}H polarization depending on the hnCE$^\pm$. Comparing these model simulations to the experimental observations we must realize that in our amorphous samples the hnCE$^\pm$ conditions are simultaneously present, meaning that these observations correspond to a collective response at all the conditions and the local-to-bulk polarization transfer. At this stage we do not yet know how to describe these combined mechanisms and to make any quantitative comparison between the experimental and simulated results. However, that in the experiment the amplitude of the recovered ^{2}H signal is rather low should be attributed to the fact that it is composed of signals, originating from the electrons at the hnCE$^\pm$ conditions, that have opposite signs and thus partially cancel each other. More experimental studies are necessary before a model system can be constructed that combines the quantum behavior around the hnCE electron pairs and the observed bulk polarizations.
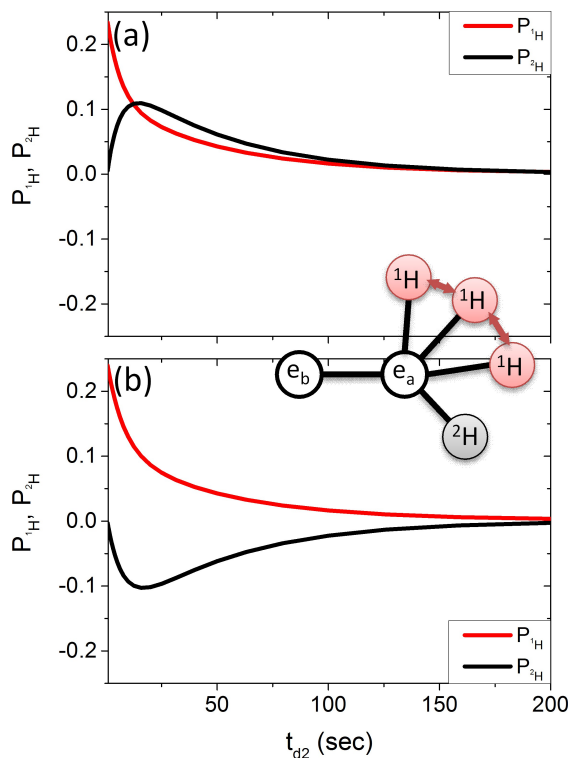
Figure 17: Simulated DNP recovery experiment where the nuclear polarization $P_{^1\mathrm{H}}(t_{d2})$ (blue) and $P_{^2\mathrm{H}}(t_{d2})$ (magenta) are plotted for the six-spin system of $\{e_a - e_b - (^1\mathrm{H}_3, {}^2\mathrm{H})\}$ at the (a) hnCE$^-$ and at the (b) hnCE$^+$ conditions. A sketch of the spin system is plotted: Two electrons, dipolar-coupled, hyperfine-coupled to three $^1\mathrm{H}$ nuclei and one $^2\mathrm{H}$ nucleus. The solid lines represent dipolar or hyperfine interactions. The red two-sided arrows represent cross-relaxation between the $^1\mathrm{H}$ nuclei. Both nuclei are prepolarized by placing $\delta\nu_{excite} = \delta\nu_a$ $(\delta\nu_a < \delta\nu_b)$ until the polarizations reached their steady state values. At $t_{d2} = 0$ the $^2\mathrm{H}$ was saturated and the polarizations of both nuclei were followed as a function of t_{d2}. After the saturation the $^2\mathrm{H}$ polarization partially recovered on account of the $^1\mathrm{H}$ polarization. The polarizations are plotted with respect to the electron polarizations at thermal equilibrium. The parameters of the calculation are: $\delta\nu_a = 0$ MHz, $\delta\nu_b = 121.9632$ MHz for hnCE$^-$ and $\delta\nu_b = 165.9737$ MHz for hnCE$^+$, $\nu_{^1\mathrm{H}} = 144$ MHz, $\nu_{^2\mathrm{H}} = 22$ MHz, $\Delta_{ab} = 3$ MHz, $A_{z,aH,i} = A_{z,bH,i} = 0$ MHz for $i = 1 - 3$, $A^{\pm}_{aH,1} = 0.5$ MHz, $A^{\pm}_{aH,2} = 0.4$ MHz, $A^{\pm}_{aH,3} = 0.45$ MHz, $A^{\pm}_{bH,i} = 0$ MHz for $i = 1 - 3$, $A^{\pm}_{aD} = 0.25$ MHz, $A^{\pm}_{bD} = 0$ MHz, $T_{1e} = 100$ msec, $T_{1,^1\mathrm{H}} = 20$ sec, $T_{1,^2\mathrm{H}} = 80$ sec, $T^H_{1d} = 1$ msec, $T_{2e} = 20$ usec, $T_{2n} = 100$ usec, $T = 10$ K, $\delta\nu_1 = 0.5$ MHz, $t_{excite} = 500$ sec, $\delta\nu_{excite} = 0$ MHz, saturation of $^2\mathrm{H}$ nucleus.

Fig. 18 shows that when we continuously saturate the $^1\mathrm{H}$ nucleus such that $P_{^1\mathrm{H}}(t_{2d}) = 0$ for all t_{2d}'s, the $^2\mathrm{H}$ polarization reaches zero on a very short time scale. This timescale is much shorter than the decay time without saturation which is of the order of $T_{1,^1\mathrm{H}}$ and thus much shorter than $T_{1,^2\mathrm{H}}$ in these simulations. This qualitatively agrees with

experiments observations in Fig. 13. The fast saturation of the ^{2}H polarization close to the hnCE electrons does not allow any buildup of bulk polarization via spin diffusion.

In conclusion we can say that the hnCE$^\pm$processes can be considered as the source of the temporal effects observed in our experiments. Further studies are necessary to quantify the observations, but the present results already indicate that these processes can play an important role in the connectivities between the polarization of the two types of nuclei.
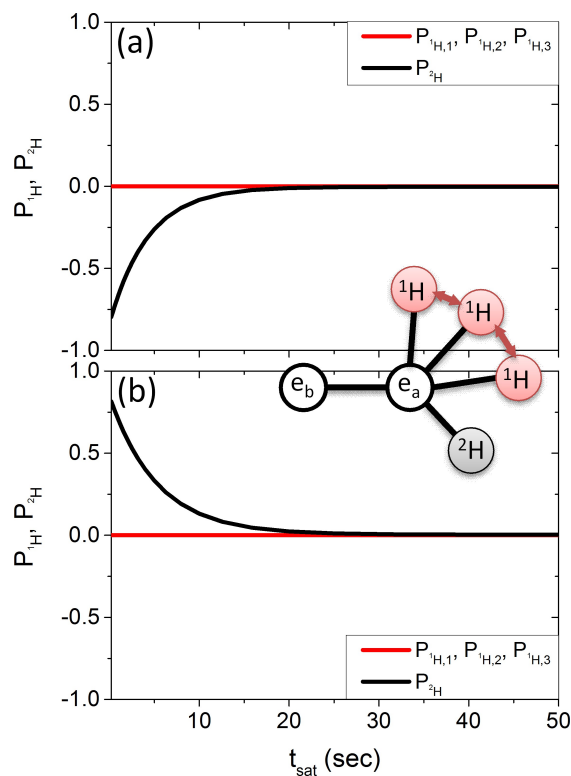
Figure 18: Simulated decay of hyperpolarized ^{2}H signal upon continuous saturation of the ^{1}H nuclei in the system. $P_{^1\text{H}}(t_{sat})$ (blue) and $P_{^2\text{H}}(t_{sat})$ (magenta) are plotted for the six-spin system of $\{e_a - e_b - (^1\text{H}_3, ^2\text{H})\}$ at the (a) hnCE$^-$ and at the (b) hnCE$^+$ conditions. A sketch of the spin system is plotted: Two electrons, dipolar-coupled, hyperfine-coupled to three ^{1}H nuclei and one ^{2}H nucleus. The solid lines represent dipolar or hyperfine interactions. The red two-sided arrows represent cross-relaxation between the ^{1}H nuclei. Both nuclei are prepolarized by placing $\delta\nu_{excite} = \delta\nu_a$ ($\delta\nu_a < \delta\nu_b$) until the polarizations reached their steady state values. At $t_{MW} = 0$ the ^{1}H was continuously saturated such that $P_{^1\text{H}}(t) = 0$ for all t_{sat}'s and the polarizations of both nuclei were followed as a function of t_{sat}. As a result of the ^{1}H saturation the ^{2}H nucleus decayed to zero within several seconds. The polarizations are plotted with respect to the electron polarizations at thermal equilibrium. The parameters of the calculation are: $\delta\nu_a = 0$ MHz, $\delta\nu_b = 121.9632$ MHz for hnCE$^-$ and $\delta\nu_b = 165.9737$ MHz for hnCE$^+$, $\nu_{^1\text{H}} = 144$ MHz, $\nu_{^2\text{H}} = 22$ MHz, $\Delta_{ab} = 3$ MHz, $A_{z,aH,i} = A_{z,bH,i} = 0$ MHz for $i = 1 - 3$, $A_{aH,1}^\pm = 0.5$ MHz, $A_{aH,2}^\pm = 0.4$ MHz, $A_{aH,3}^\pm = 0.45$ MHz, $A_{bH,i}^\pm = 0$ MHz for $i = 1 - 3$, $A_{aD}^\pm = 0.25$ MHz, $A_{bD}^\pm = 0$ MHz, $T_{1e} = 100$ msec, $T_{1,^1\text{H}} = 20$ sec, $T_{1,^2\text{H}} = 80$ sec, $T_{1d}^H = 1$ msec, $T_{2e} = 20$ usec, $T_{2n} = 100$ usec, $T = 10$ K, $\delta\nu_1 = 0.5$ MHz, $t_{excite} = 500$ sec, $\delta\nu_{excite} = 0$ MHz, saturation of ^{1}H nucleus, $t_{RF} = 100$ sec.

5 Discussion and Conclusions

In our "H$_2$O" sample we observed that the frequency dependent ^{1}H DNP enhancement lineshapes at 6 and 20 K can be derived from the electron polarization profiles resulting from the MW and spectral diffusion as expected from the ^{1}H-iCE. However, while at 20 K the ^{2}H DNP polarizations can be described by the ^{2}H-iCE process, their steady state values at 6K are coupled to the ^{1}H polarization.

We should comment here that the similar maximal enhancements observed at 20K for the bulk ^{1}H and ^{2}H polarizations can be expected, when the ^{1}H and ^{2}H iCE-DNP processes are the dominant mechanisms and the shape of the electron polarization determining the DNP enhancement is smooth, and we could ignore differences between $T_{1,^1H}$ and $T_{1,^2H}$ and the number of nuclei per unit of volume influencing the bulk polarizations. This is simply due to the fact that the source of the enhancements is the electron polarization differences $\{P_{b_x}(\delta\nu_{b_x}) - P_{a_x}(\delta\nu_{a_x})\}_{^xH}$ of the ^xH-iCE electrons a_x and b_x for $x = 1, 2$, which on average are expected to be proportional to the frequency separations with $(\delta\nu_{b_1} - \delta\nu_{a_1})/(\delta\nu_{b_2} - \nu_{a_2}) = \gamma_{^1H}/\gamma_{^2H}$.

For the 6K case our experiments on the "H$_2$O" sample show that the ^{1}H and the ^{2}H enhancements, ϵ_{2H} and ϵ_{2H}, are about equal at all $\delta\nu_{excite}$ values

$$\epsilon_{^1H}(\delta\nu_{excite}) = \epsilon_{^2H}(\delta\nu_{excite}), \tag{16}$$

That this equilibration at 6 K can not be described by the standard TM mechanism was discussed in Section 4. As mentioned above the values of $\epsilon_{^1H}(\delta\nu_{excite})$ are determined by the electron polarization profiles via the ^{1}H-iCE and reach an overall steady state in a timescale that is of the order of $T_{bu,^1H}$. This time is significantly shorter than the time it takes for $\epsilon_{^2H}(\delta\nu_{excite})$ to reach its steady state values. This discrepancy in timescales led us to the conclusion that the source of the ^{2}H-to-^{1}H polarization equilibration process must take place at distinct sites in the sample and that the bulk ^{2}H nuclei are still polarized by spin diffusion. At these sites an exchange of polarization must be possible presumably mediated by coupled electrons. From the similarity between the time dependent experiments in Section 3.2 and the simulations in Section 4.3 it is apparent that the hnCE electron spin pairs can play an important role in the cross-talk between the two nuclear spin types. The complexity of the correlation between the local ^{1}H and ^{2}H polarizations at the hnCE sites can be appreciated when following the discussion in Section 4.3.1 for the (II) $\{e_c - e_a - e_b - (^1H_3,^2H) - e_d\}$ spin system. Close to these spin pairs there exists a strong nuclear state mixing together with an electron state mixing which form a source of mutual dependence between the two nuclear polarizations. In particular we showed that at a simple hnCE site $\{e_a - e_b - (^1H_3,^2H)\}$ with a fixed ^{1}H polarization the ^{2}H polarization becomes about equal to the plus or minus the ^{1}H polarization. Thus

49

this could mean that the hnCE electron pairs are the sites of polarization exchange. The different sites result in different (positive and negative) local ^2H polarizations that then together are the source of the bulk polarization.

Assuming the hnCE is the correct approach for explaining our experimental results, there still remain many open questions such as the dynamics of the process and the role of the temperature. At this point we do not yet know how to model the bulk behavior and we need more experimental data to characterize the equilibration of the bulk enhancements.

Acknowledgments

References

[1] C. Jefferies, Phys. Rev. 106, (1957), 164

[2] C. Jefferies, Phys. Rev. 106, (1957), 164 A. Abragam and M. Goldman, Reports on Progress in Physics 41 (1978), 395-467

[3] T. J. Schmugge and C. D. Jeffries, Phys. Rev., 1965, 138, A1785

[4] C.D. Jeffries, Dynamic Nuclear Orientation (Interscience, New York, 1963)

[5] A. Abragam and W. G. Proctor, Phys. Rev., 1958, 109, 1441

[6] M. Borghini and A. Abragam, Compt. Rend., 1959, 203, 1803

[7] O. S. Leifson and C. D. Jeffries, Phys. Rev., 1961, 122, 1781

[8] R. A. Wind, M. J. Duijvestijn, C. van der Lugt, A. Manenschijn and J. Vriend, Prog. Nucl. Magn. Reson. Spectrosc., 1985, 17, 33-67

[9] Y. Hovav, A. Feintuch and S. Vega, J. Chem. Phys., 2011, 134, 074509

[10] T. Maly, G. T. Debelouchina, V. S. Bajaj, K. Hu, C. Joo, M. L. Mak-Jurkauskas, J. R. Sirigiri, P. C. A. van der Wel, J. Herzfeld, R. J. Temkin and R. G. Griffin, J. Chem. Phys., 2008, 128, 052211

[11]　C. F. Hwang and D. A. Hill, Phys. Rev. Lett. 18,(1967), 110

[12]　C. F. Hwang and D. A. Hill, Phys. Rev. Lett. 19,(1967), 1011

[13]　D. S. Wollan, Phys.Rev.B, 1976, 13, 3671-3685

[14]　A. V. Kessenikh, V. I. Lushchikov, A. A. Manenkov, Y. V. Taran, Sov. Phys. Solid State, 1963, 5, 321−329

[15]　A. V. Kessenikh, V. I. Luschikov and A. A. Manenkov, Phys. Solid State, 1963, 5, 835–837

[16]　A. V. Kessenikh, A. A. Manenkov, G. I. Pyatnitskii, Sov. Phys. Solid State, 1964, 6, 641–643

[17]　Y. Hovav, A. Feintuch and S. Vega, Journal of Magnetic Resonance, 2012, 214, 29-41

[18]　K. Hu, G. T. Debelouchina, A. A. Smith and R. G. Griffin, J. Chem. Phys., 2011, 134, 125105

[19]　Y. Hovav, D. Shimon, I. Kaminker, A. Feintuch, D. Goldfarb and S. Vega, Physical Chemistry Chemical Physics, 2015, 17, 6053-6065.

[20]　A. Abragam, Principles of Nuclear Magnetism (Clarendon Press, Oxford, 1961)

[21]　S. A. Dzuba and A. Kawamori, Concepts Magn. Reson., 1996, 8, 49-61

[22]　K. M. Salikhov, Yu D. Tsvetkov, in Time Domain Electron Spin Resonance. L. Kevan, R.N. Schwartz (Wiley-Interscience, New York 1979)

[23]　Y. Hovav, I. Kaminker, D. Shimon, A. Feintuch, D. Goldfarb and S. Vega, PCCP, 2015, 17, 226-244

[24]　T. A. Siaw, M. Fehr, A. Lund, A. Latimer, S. A. Walker, D. T. Edwards and S. Han, Physical Chemistry Chemical Physics, 2014, 16, 18694-18706

[25]　J. Granwehr and W. Kockenberger, Applied Magnetic Resonance, 2008, 34, 355-378.

[26]　V. A. Atsarkin, G. A. Vasneva and E. Novikov, J. Exp. Theor. Phys., 1975, 41(4), 746−751

[27]　A. Abragam and M. Borghini, Progress in Low Temperature Physics (North-Holland, Amsterdam, 1964), Vol. 4

[28]　M. Borghini and K. Scheffler, Phys. Rev. Lett., 1971, 26, 1362-1365

[29]　V. A. Atsarkin, Soviet Journal of Experimental and Theoretical Physics, 1971, 32, 421

[30] A. G. Redfield, Phys. Rev., 1955, 98, 1787-1809

[31] B. N. Provotorov, Soviet Phys. JETP, 1962, 14, 1126-1131

[32] V. A. Atsarkin and A. V. Kessenikh, Applied Magnetic Resonance, 2012, 43, 7-19

[33] M. Borghini, Phys. Rev. Lett., 1968, 20(9), 419–421

[34] M. Goldman, Spin temperature and nuclear magnetic resonance in solids, (Clarendon Press, Oxford, 1970)

[35] K. H. Hausser and D. Stehlik, Dynamic Nuclear Polarization in Liquids, Adv. Magn. Opt. Reson., 1968, 3, 79-139

[36] V. Denysenkov, M. J. Prandolini, M. Gafurov, D. Sezer, B. Endeward and T. F. Prisner, Liquid state DNP using a 260 GHz high power gyrotron, Phys. Chem. Chem. Phys., 2010, 12, 5786-5790

[37] M. Gafurov, V. Denysenkov, M. J. Prandolini and T. F. Prisner, Temperature Dependence of the Proton Overhauser DNP Enhancements on Aqueous Solutions of Fremy's Salt Measured in a Magnetic Field of 9.2 T, Appl. Magn. Reson., 2012, 43, 119-128

[38] P. Neugebauer, J. G. Krummenacker, V. P. Denysenkov, C. Helmling, C. Luchinat, G. Parigi and T. F. Prisner, High-field liquid state NMR hyperpolarization: A combined DNP/NMRD approach, Phys. Chem. Chem. Phys., 2014, 16, 18781-18787

[39] T. Can, M. Caporini, F. Mentink-Vigier, B. Corzilius, J. Walish, M. Rosay, W. Maas, M. Baldus, S. Vega and T. Swager, J. Chem. Phys., 2014, 141, 064202

[40] J. Z. Hu, J. Zhou, B. Yang, L. Li, J. Qiu, C. Ye, M. S. Solum, R. A. Wind, R. J. Pugmire and D. M. Grant, Solid State Nucl. Magn. Reson., 1997, 8, 129-137.

[41] A. W. Overhauser, Phys. Rev., 1953, 92, 411

[42] T. R. Carver and C. P. Slichter, Phys. Rev., 1953, 92, 212

[43] A. Abragam, Overhauser Effect in Nonmetals, Phys. Rev., 1955, 98, 1729-1735

[44] L. H. Bennett and H. C. Torrey, Phys. Rev., 1957, 108, 499

[45] L. Lumata, A. K. Jindal, M. E. Merritt, C. R. Malloy, A. D. Sherry and Z. Kovacs, J. Am. Chem. Soc., 2011, 133, 8673-8680

[46] F. Kurdzesau, B. van den Brandt, A. Comment, P. Hautle, S. Jannin, J. J. van der Klink and J. A. Konter, J. Phys. D-Appl. Phys., 2008, 41, 155506

[47] S. Jannin, A. Comment, F. Kurdzesau, J. Konter, P. Hautle, B. van den Brandt and J. J. van der Klink, J. Chem. Phys., 2008, 128(24), 241102

[48] C. T. Farrar, D. A. Hall, G. J. Gerfen, S. J. Inati and R. G. Griffin, J. Chem. Phys., 2001, 114, 4922-4933

[49] S. Jannin, A. Comment and J. van der Klink, Applied Magnetic Resonance, 2012, 43, 59-68

[50] L. Lumata, M. E. Merritt, C. R. Malloy, A. D. Sherry and Z. Kovacs, The Journal of Physical Chemistry A, 2012, 116, 5129-5138.

[51] W. de Boer, M. Borghini, K. Morimoto, T. O. Niinikoski and F. Udo, J. Low Temp. Phys., 1974, 15, 249-267

[52] W. de Boer, J. Low Temp. Phys., 1976, 22, 185-212

[53] P. Miéville, P. Ahuja, R. Sarkar, S. Jannin, P. Vasos, S. Gerber-Lemaire, M. Mishkovsky, A. Comment, R. Gruetter, O. Ouari, P. Tordo and G. Bodenhausen, Angew. Chem. Int. Edit., 2010, 49, 6182-6185.

[54] A. Bornet, R. Melzi, S. Jannin and G. Bodenhausen, Applied Magnetic Resonance, 2012, 43, 107-117.

[55] A. Bornet, R. Melzi, A. J. Perez Linde, P. Hautle, B. van den Brandt, S. Jannin and G. Bodenhausen, The Journal of Physical Chemistry Letters, 2012, 4, 111-114.

[56] L. Lumata, M. Merritt, C. Malloy, A. D. Sherry and Z. Kovacs, Applied Magnetic Resonance, 2012, 43, 69-79

[57] L. L. Lumata, M. E. Merritt, C. R. Malloy, A. D. Sherry, J. van Tol, L. Song and Z. Kovacs, J. Magn. Reson., 2013, 227, 14-19

[58] T. A. Siaw, S. A. Walker, B. D. Armstrong and S. Han, Journal of Magnetic Resonance, 2012, 221, 5-10.

[59] D. Shimon, Y. Hovav, A. Feintuch, D. Goldfarb and S. Vega, Phys. Chem. Chem. Phys., 2012, 14, 5729-5743

[60] D. Shimon, A. Feintuch, D. Goldfarb and S. Vega, Phys. Chem. Chem. Phys., 2014, 16, 6687-6699

[61] D. Shimon, Y. Hovav, I. Kaminker, A. Feintuch, D. Goldfarb and S. Vega, Phys. Chem. Chem. Phys., 2015, 17, 11868-11883

[62] J. H. Ardenkjaer-Larsen, S. Macholl and H. Johannesson, Appl. Magn. Reson. (Austria), 2009, 34, 509; 509-522; 522.

[63] H. Jóhannesson, S. Macholl and J. H. Ardenkjaer-Larsen, Dynamic Nuclear Polarization of [1-13C]pyruvic acid at 4.6 tesla, J. Magn. Reson., 2009, 197, 167-175.

[64] D. Banerjee, D. Shimon, A. Feintuch, S. Vega and D. Goldfarb, J. Magn. Reson., 2013, 230, 212-219

[65] F. M. Vigier, D. Shimon, V. Mugnaini, J. Veciana, A. Feintuch, M. Pons, S. Vega and D. Goldfarb, Phys. Chem. Chem. Phys., 2014, 16, 19218-19228

[66] Ü. Akbey, F. Camponeschi, B. van Rossum and H. Oschkinat, ChemPhysChem, 2011, 12, 2092-2096.

[67] S. F. J. Cox and V. Bouffard and M. Goldman, Journal of Physics C: Solid State Physics, 1973, 6, L100

[68] I. J. Day, J. C. Mitchell, M. J. Snowden and A. L. Davis, Magn. Reson. Chem., 2007, 45, 1018-1021

[69] F. Blanc, L. Sperrin, D. A. Jefferson, S. Pawsey, M. Rosay and C. P. Grey, J. Am. Chem. Soc., 2013, 135, 2975-2978

[70] O. Lafon, M. Rosay, F. Aussenac, X. Lu, J. Trébosc, O. Cristini, C. Kinowski, N. Touati, H. Vezin and J. Amoureux, Angew. Chem. Int. Edit., 2011, 50, 8367-8370

[71] O. Lafon, A. S. L. Thankamony, M. Rosay, F. Aussenac, X. Lu, J. Trebosc, V. Bout-Roumazeilles, H. Vezin and J. Amoureux, Chem. Commun., 2013, 49, 2864-2866

[72] S. Reynolds and H. Patel, Appl. Magn. Reson., 2008, 34, 495-508

[73] A. Feintuch, D. Shimon, Y. Hovav, D. Banerjee, I. Kaminker, Y. Lipkin, K. Zibzener, B. Epel, S. Vega and D. Goldfarb, J. Magn. Reson., 2011, 209, 136-141

[74] Y. Hovav, A. Feintuch and S. Vega, J. Chem. Phys., 2011, 134, 074509

[75] D. A. Erilov, R. Bartucci, R. Guzzi, A. A. Shubin, A. G. Maryasov, D. Marsh, S. A. Dzuba and L. Sportelli, The Journal of Physical Chemistry B, 2005, 109, 12003-12013.

[76] S. C. Serra, A. Rosso and F. Tedoldi, Phys. Chem. Chem. Phys., 2013, 15, 8416-8428.

[77] A. A. Smith, B. Corzilius, A. B. Barnes, T. Maly and R. G. Griffin, J. Chem. Phys., 2012, 136.

[78] M. Batel, A. Däpp, A. Hunkeler, B. H. Meier, S. Kozerke and M. Ernst, Physical Chemistry Chemical Physics, 2014, 16, 21407-21416. b

[79] 1 E. Ravera, D. Shimon, A. Feintuch, D. Goldfarb, S. Vega, A. Flori, C. Luchinat, L. Menichetti and G. Parigi, Phys. Chem. Chem. Phys., 2015, 17, 26969-26978.